NASA Conference Publication 10024

Research in Structures, Structural Dynamics and Materials 1989

Compiled by
William F. Hunter
NASA Langley Research Center
Hampton, Virginia

Ahmed K. Noor
The George Washington University
Joint Institute for Advancement of Flight Sciences
NASA Langley Research Center
Hampton, Virginia

April 1989

NASA
National Aeronautics and
Space Administration

Langley Research Center
Hampton, Virginia 23665-5225

FOREWORD

This document contains a collection of eight papers presented at the AIAA/ASME/ASCE/ AHS/ASC 30th Structures, Structural Dynamics and Materials Conference held in Mobile, Alabama, April 3-5, 1989. The conference had a total of 278 papers, including 249 full-length papers, 17 papers in special and panel sessions, and 12 short presentations in the work-in-progress sessions. Seven of the papers appearing in this document were presented in the two work-in-progress sessions and the eighth paper was presented in one of the panel sessions. Most of the full length papers are contained in the conference proceedings published by AIAA.

The fields covered by the conference are rapidly changing, and if new results and antici-pated future directions are to have maximum impact and use, it is imperative that they reach workers in the field as soon as possible. This consideration led to the decision to publish these proceedings prior to the conference. Special thanks go to the Research Information and Applica-tions Division at NASA Langley Research Center for their cooperation in publishing this volume.

The use of trademarks or manufacturers' names does not constitute endorsement, either expressed or implied, by the National Aeronautics and Space Administration.

William F. Hunter
Ahmed K. Noor
Compilers

CONTENTS

A STUDY OF COMPOSITE PLATES WITH HOLES/INCLUSIONS

Ronald Bense and Ozden Ochoa

Mechanical Engineering Department
Texas A&M University
College Station, Texas 77843

MODEL DESCRIPTION

Delamination characterization of a plate with a hole/inclusion is presented. A closed form solution is developed to obtain stresses on the boundary of hole/inclusion in the plate. Once the location with highest tangential stress is identified, FEM analysis of a laminate under tensile loading is considered. The models for the closed form and FEM are given in Figure 1 A & B. The examples are for $[\pm 35/0/90]_s$ laminate of AS4/3501-6. Tensile, Biaxial and Shear loads are considered.
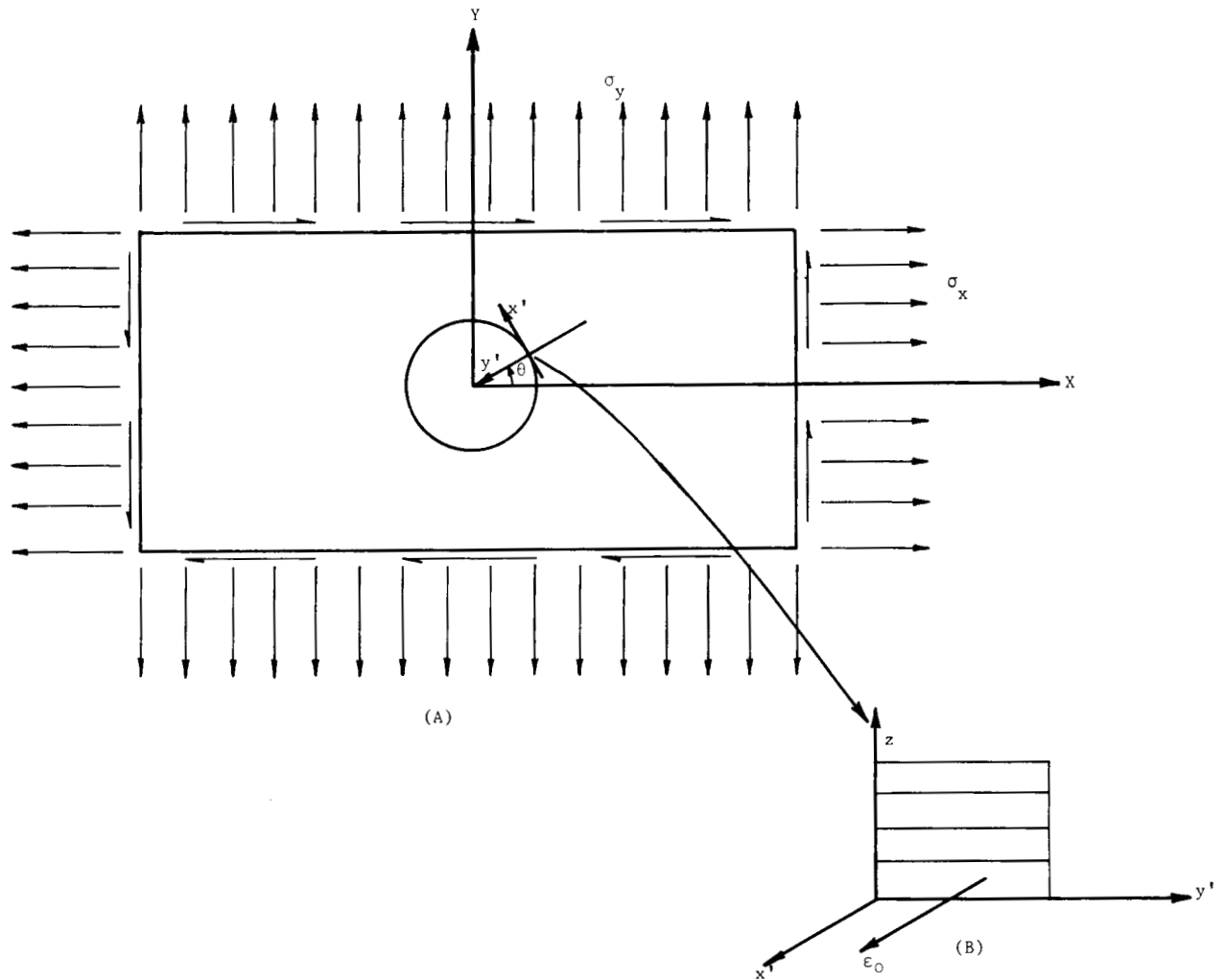
Figure 1

PROCEDURE

The analysis procedure is summerized in the following figure. The combination of closed-form (CFH - closed-form, hole [1] and CHI - closed-form, inclusion [2]) and FEM [3] solutions provide efficiency and economy in the interpretation of results.

Note: CLT is a Classical Laminate Plate Theory Algorithm

Closed Form Solution

Material Properties
Layup, Loading

Hole   Laminate Stiffness   Inclusion

CFI

CFI

CLT

$$\begin{Bmatrix} \varepsilon_0 \\ \kappa \end{Bmatrix} = \begin{bmatrix} A & B \\ \hline B & D \end{bmatrix}^{-1} \begin{Bmatrix} N \\ M \end{Bmatrix}$$

θ, σ_θ

θ, σ_θ

ε_{ox}

FEM
Free Edge Stress Analysis

$\sigma_{zz}, \sigma_{zy}, \sigma_{zx}$

FEM

Fracture Analysis Crack at the interface with highest stresses

Strain Energy Release Rates

Figure 2.

5
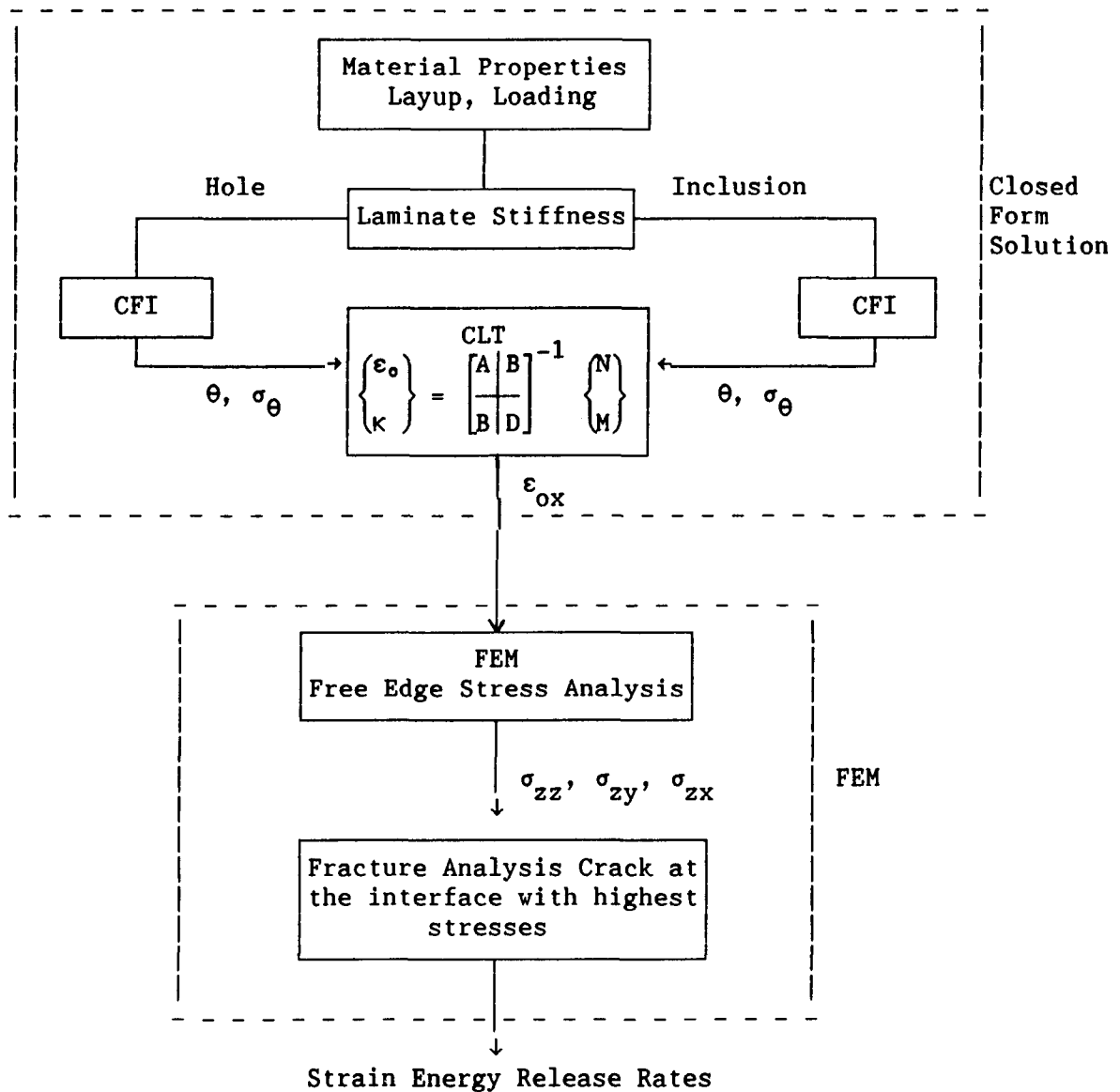
INPLANE STRAIN/STRESS RESULTS

$[\pm 35/0/90]_s$ laminate is subjected to 5000 psi axial stress. The response of this laminate with a hole and with inclusions are tabulated below. The tangential stress is obtained from the closed-form solution and the strain is evaluated from CLT.

	E inclusion/ E plate	σ_θ / σ applied	ε_o
hole (w/o inclusion)	0	3.280	$1710\mu\varepsilon$
with soft inclusion (epoxy)	.169	1.865	$972\mu\varepsilon$
with rigid inclusion (steel)	3.128	.724	$377\mu\varepsilon$

Figure 3

TANGENTIAL STRESS AROUND THE HOLE BOUNDARY

The tangential stress field for a laminate with a hole subjected to uniaxial tension and shear is presented in Figure 4. These stresses are displayed as a function of θ around the boundary of the hole. As can be observed, the highest tangential stress is at $\theta = 90°$ for the tensile load and $\theta = 50.5°$ for the shear load.
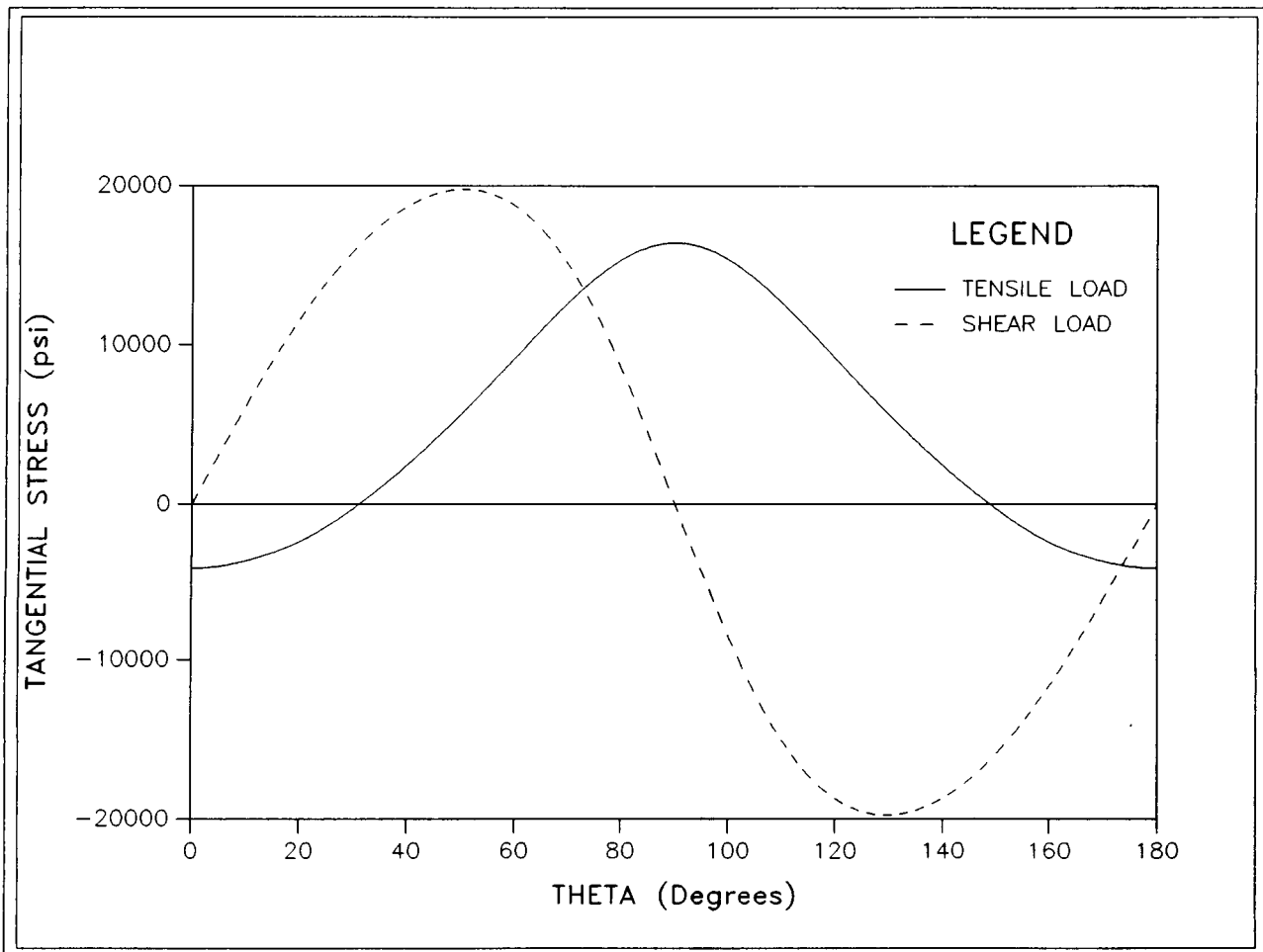
Figure 4

INTERLAMINAR NORMAL STRESS VARIATION

The closed-form reslults of Figure 4 are converted to applied tensile strain, ε_{ox} = 1710με to be used in the FEM calculations. The FEM analysis models the laminate cross-section through-the-thickness and evaluates the interlaminar normal and shear stresses. Figure 5 presents the variation of the interlaminar normal stress along the y axis for each interface. Note that high stresses are at the free edge, between the 90/90 laminae and the 0/90 laminae.
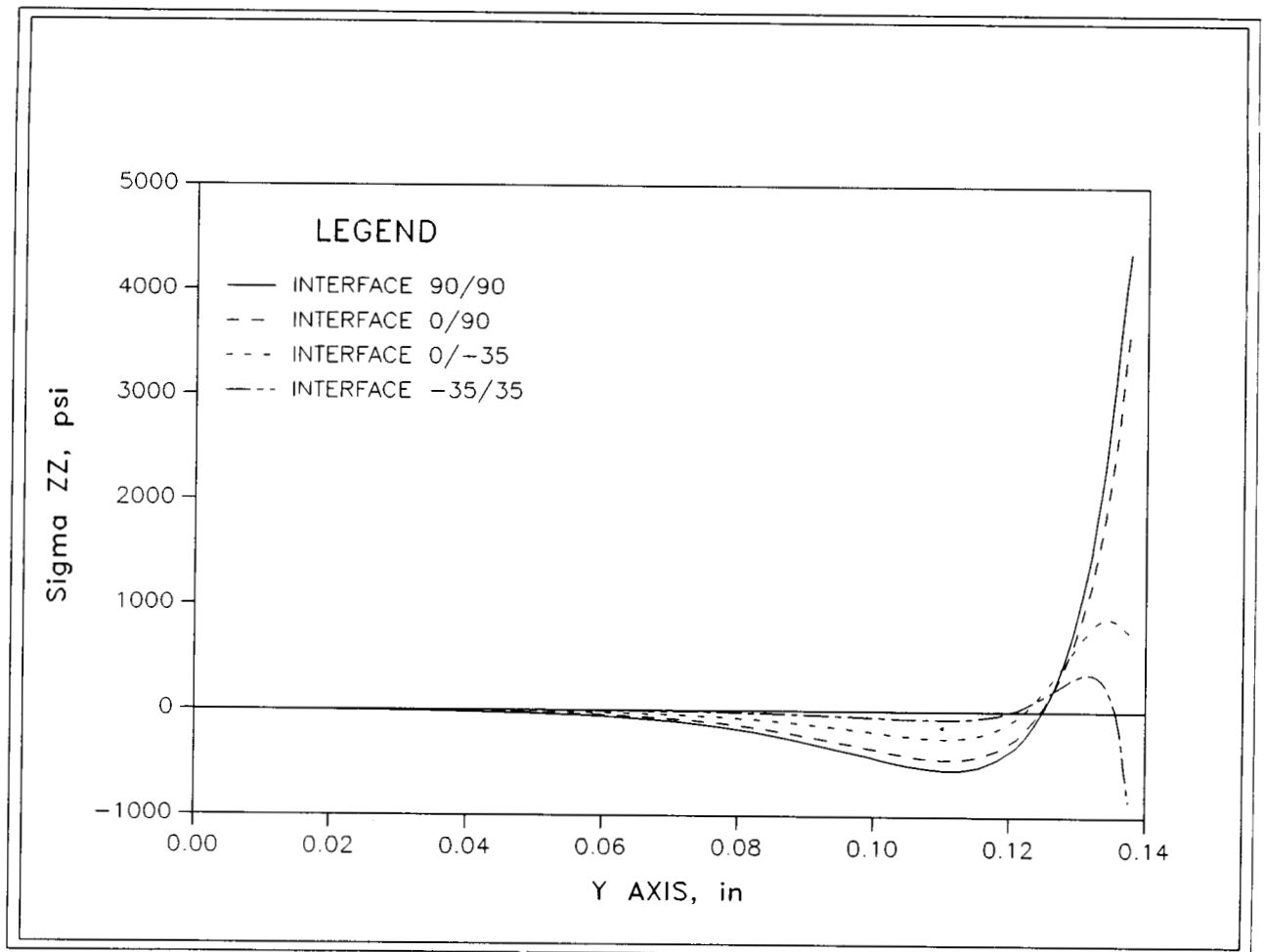
Figure 5

INTERLAMINAR SHEAR STRESSES

    Figure 6 presents the variation of the interlaminar shear stresses, σ_{zx} and
σ_{zy}, along the Y-axis for each interface. It should be observed that the
highest σ_{zx} is at the free edge between the -35/35 laminae and that σ_{zx} rapidly
vanishes inside the laminate. Note that the highest σ_{zy} is just inside the
laminate near the free edge between the 0/-35 laminae.

Figure 6
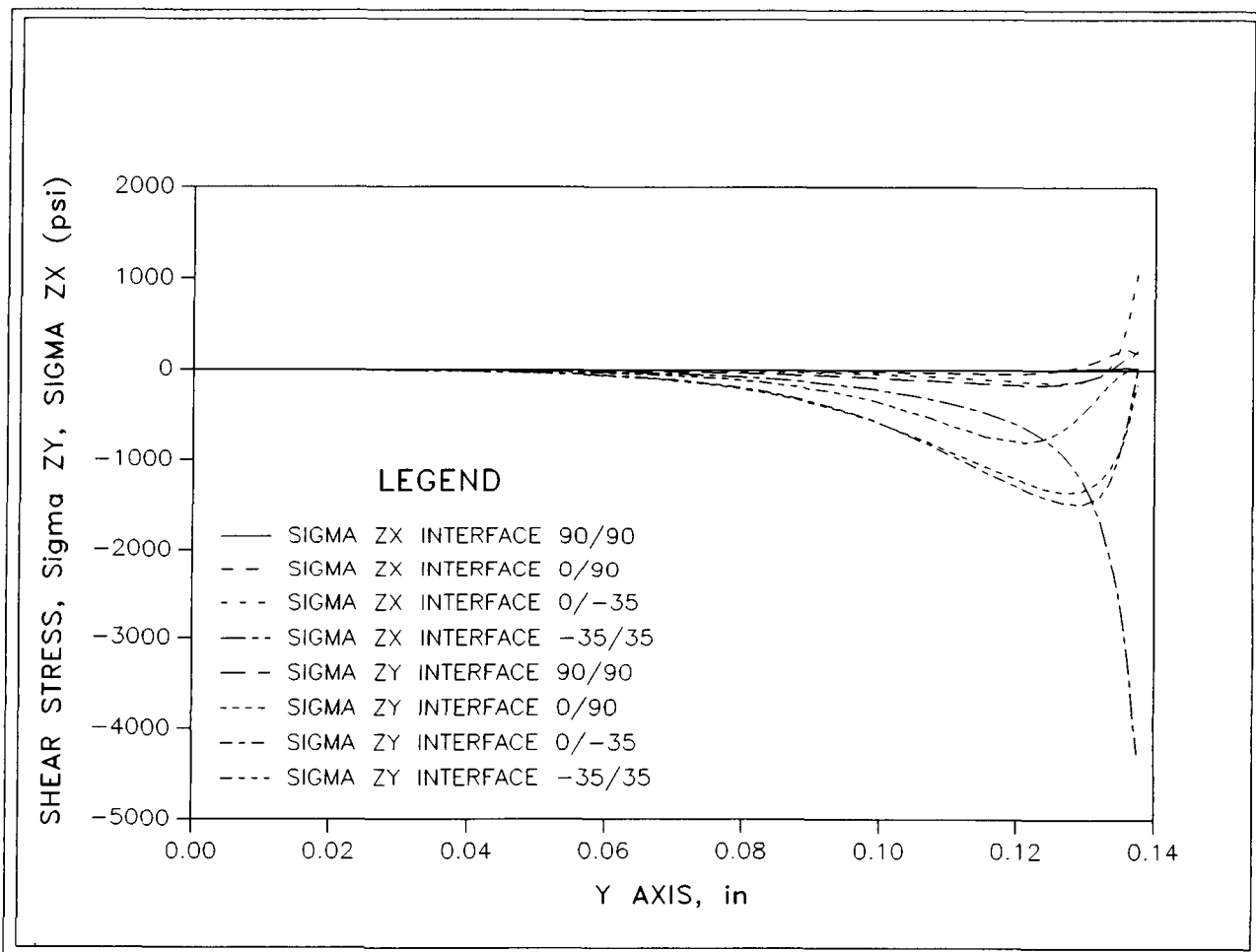
Figure 7 presents a comparison of the relative magnitudes of σ_{zz}, σ_{zx}, σ_{zy} at the free edge through the thickness. As can be observed, σ_{zy} is much smaller than σ_{zz} and σ_{zx}. σ_{zz} is relatively large at the midplane, 90/90, and at the first interface, 0/90. The shear stress σ_{zx} is highest at the third interface, -35/35. The fourth interface is the top surface of the laminate and has no interlaminar stresses.

The strain energy release rates for this laminate are evaluated by modeling a crack of a length equal to the thickness of 8 plies at the 0/90 interface. The resulting ratios are $G_I/_{GTOT}$ = .94096 and $G_{II}/_{GTOT}$ = .05827, indicating that Mode I behavior is dominant.
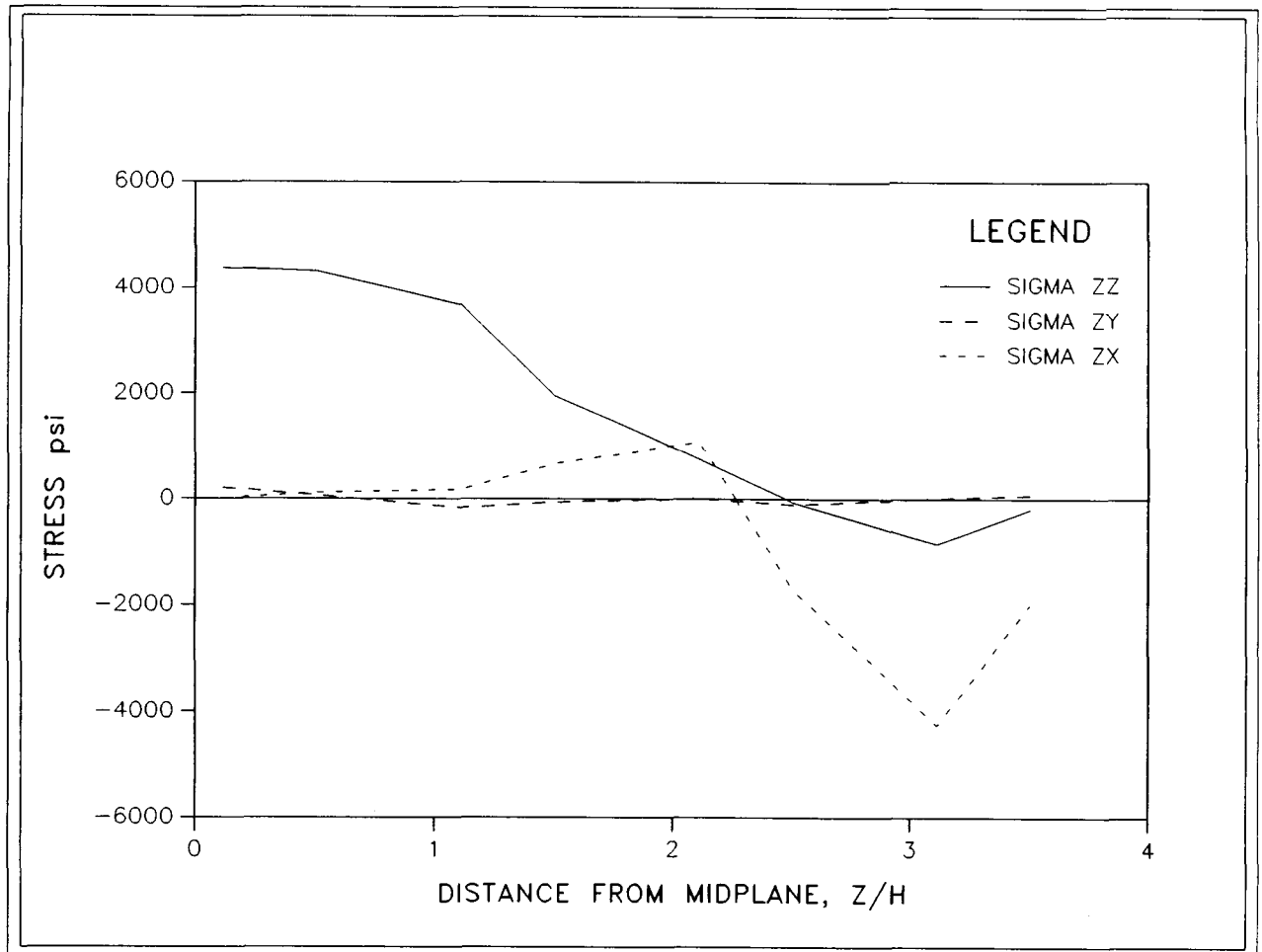
Figure 7

DEFORMATION OF HOLE/INCLUSION BOUNDARY

The effects of inclusion moduli on deformation are displayed in Figure 8. As expected a soft inclusion results in larger displacements. The $[\pm 35/0/90]_s$ laminate is loaded with uniaxial tensile stress of 50 ksi. The inclusion diameter is .5 inches.
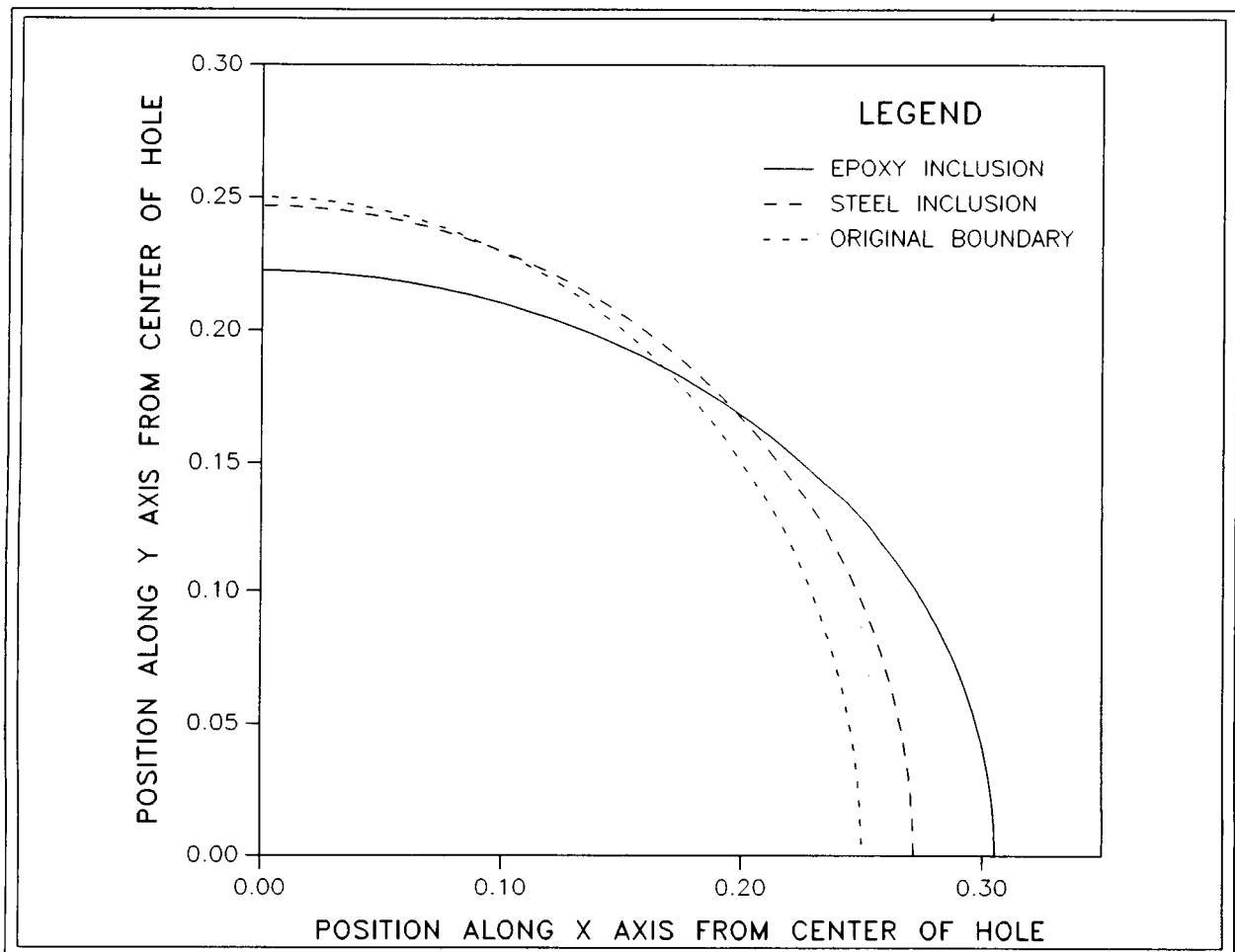
Figure 8

REFERENCES

1. S.C. Tan, "Composite Laminates Containing an Elliptical Opening," <u>J. of Composite Materials</u>.

2. S.G. Lekhnitskii, <u>Anisotropic Plates</u>, pp.190-218.

3. W.S. Chan and O.O. Ochoa, "Suppression of Edge Delamination In Composite Laminates By Terminating a Critical Ply Near the Edges," presented at the AIAA 29th SDM Conference, 1988.

12

LOCAL STIFFENER AND SKIN POCKET BUCKLING PREDICTION
BY SPECIAL PASCO MODELING TECHNIQUE:
CORRELATION TO TEST DATA

Dah N. Yin, Vu M. Tran, and Patrick M. Swift
Rockwell International, Space Transportation Systems Division
Downey, California

INTEGRALLY MACHINED WAFFLE PANELS

Waffle panels are often used on fuselage shell structures such as that of the Space Shuttle. There are a number of advantages to using waffle paneling. The waffle panel design is an efficient design for carrying biaxial, in-plane and shear loads. The geometry of the waffle panel pockets can be adjusted to account for variability of loading in the principle directions. The stiffeners of the waffle panel readily provide attachment support for secondary systems, an important consideration for aerospace structures. The waffle panel also represents the simplest integrally machined panel design to manufacture. Figure 1 shows a typical waffle panel design. The integrally machined waffle panel is constructed with a fillet radius between the vertical stiffener and the plate. This fillet radius provides additional stability and load carrying capability to the structure. Present analysis techniques for waffle type structures include classical theory of plate buckling, introduced here as the Rockwell-developed program WAFFLE, and the NASA-developed stress analysis program--Panel Analysis and Sizing Code (PASCO). This paper discusses the application of the PASCO program in conjunction with the WAFFLE program to account for both the fillet radius and the presence of stiffeners in both directions. The results of the tests are used to verify that these adjustments are valid and necessary if accurate analysis of the waffle panel is to be achieved.
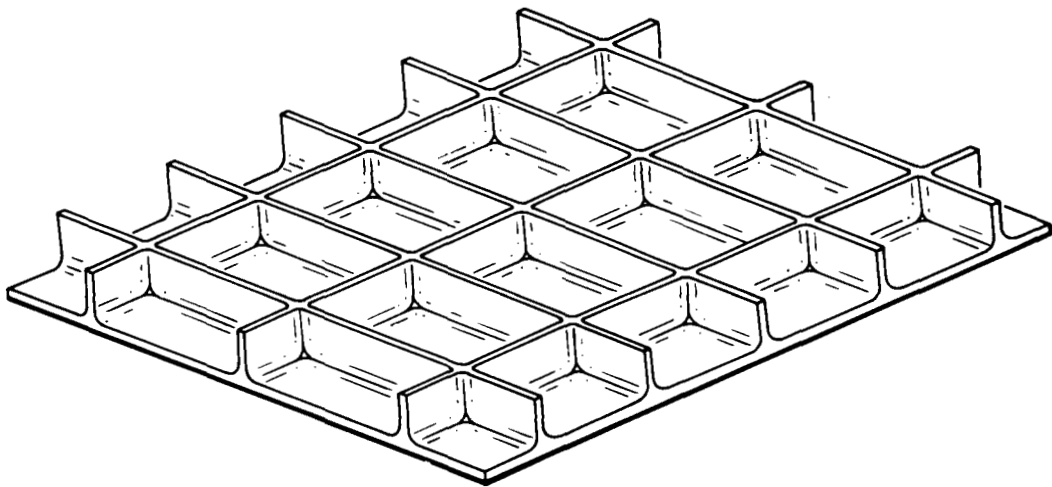
Figure 1

THE WAFFLE PROGRAM

The WAFFLE program was developed at Rockwell for application on waffle panels. It is based on NACA Technical Notes (refs. 1, 2, 3, 4, and 5). The critical stresses are determined on the basis of the principle that during buckling, the elastic strain energy stored in a structure is equal to the work done by the applied loads. The deflection function is expressed exactly by means of a two-dimensional infinite Fourier series. The Raleigh-Ritz method is applied to obtain an infinite set of homogeneous linear equations needed to solve for the Fourier coefficients. The solutions of these equations that give Fourier coefficients not all equal to zero exist only for those combinations of shear and direct stress for which the buckled plate is in neutral equilibrium. The matrix iteration method was then applied to solve for the 10 most important equations that best satisfy the loading condition. Input load includes in-plane and moment loads in both directions, shear loading, and lateral pressure. Thermal stress caused by temperature gradients is also calculated. The effect of the combined loadings is reflected in the general instability margin of safety. Local instability of the waffle panel is also taken into account by computing the crippling and buckling allowables of the stiffener as well as pocket skin buckling allowable (ref. 6). It should be noted that although it is the same plate buckling theory that is used to obtain the buckling allowable of the whole panel as well as the buckling allowable of the pocket skin, the bending stiffness formulation of the former reflects the orthotropic effects presented by the biaxial stiffeners. WAFFLE therefore represents a comprehensive stress analysis of the waffle panel. Figure 2 shows a sample output of the program.

COMPRESSION TEST

PANEL GEOMETRY AND PROPERTIES AT 70. DEG. TEMPERATURE:

A = 20.00	B = 18.00	BSX = 4.00	BSY = 3.00
TS = .0660	H = .800	TWX = .086	TWY = .086
TEX = .0921	TEY = .0856	IX = .003530	IY = .002775
RAD = .1875	FCY = 57037.	E = 10.9E + 06	

APPLIED LOADS: (+ IS COMPRESSION AND – IS TENSION)

NX = 2000.	NY = 0.	NXY = 0.	PRESS = .00
TEMP = 70.0	TDX = .00	TDY = .00	

POCKET STABILITY: (LBS/IN.)

NXP = 1434.	NYP = 0.	NXYP = 0.	M.S. = –.03

STIFFENER STABILITY: (PSI)

FCSX = 21722.	FCWX = 21722.	M.S. = 1.48
FCSY = 0.	FCWY = 0.	(NO LOADS)

GENERAL STABILITY:

GRX = .9010	GRXY.0000	M.S. = ,.11
RTX = .0000	RTV .0000	

Figure 2

THE PASCO PROGRAM

The PASCO program was developed by M.S. Anderson and W.J. Stroud of NASA. It was designed for analyzing and sizing uniaxially stiffened panels. Buckling and vibration analyses are carried out with a linked plate analysis computer code denoted VIPASA, which is incorporated into PASCO (refs. 7, 8, and 9). Typical loading conditions for an uniaxially stiffened panel include longitudinal and transverse loads, shear load, bending moment, lateral pressure, temperature, and a bow-type imperfection (fig. 3). PASCO ordinarily models a cross section by assuming there is a repetition of substructures. The substructure is composed of an arbitrary assemblage of thin, flat, rectangular plate elements that are connected together along their longitudinal edges. The loads on each plate element are calculated under the assumption of uniform longitudinal strain. In addition, transverse load is assumed to be carried by the skin elements.
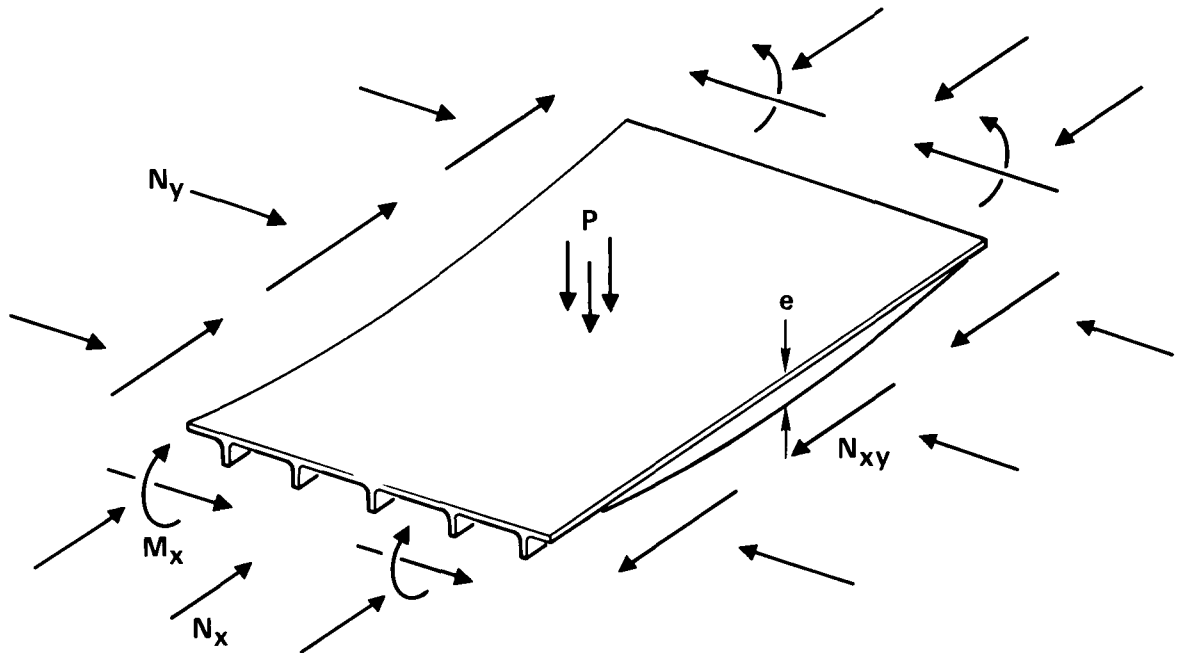

Figure 3

PASCO MODELS

PASCO's capability is limited to uniaxially stiffened panels. Biaxially stiffened panels such as waffle panels, however, can be analyzed by assuming that the waffle is made up of a series of uniaxially stiffened panels whose interface lines are the location of the transverse stiffeners. Boundary conditions along the longitudinal edges can be simply supported or clamped. Boundary conditions can not be prescribed on the ends (transverse edges) of the panel. PASCO, however, implicitly assumes that the end lines remain straight after buckling. Thus, in effect, PASCO imposes a simply support condition on the ends. Since the real waffle panel behaves neither as simply supported or clamped edge condition at the interface lines, we would expect a conservative result. A more accurate model would apply a bending moment at the interface. This bending moment can be determined from WAFFLE program. Additional loading because of the thermal gradient could indirectly be determined by WAFFLE and be input into PASCO. Two PASCO models were run and the results were compared with the actual test result. Panel geometry, loading, and boundary conditions similar to the actual test were made. In one of the PASCO models, five small elements stacked on top of each other simulated the fillet radii. The total area of these elements added up to the total area of the real fillet. Plots of the two models are shown in figure 4.
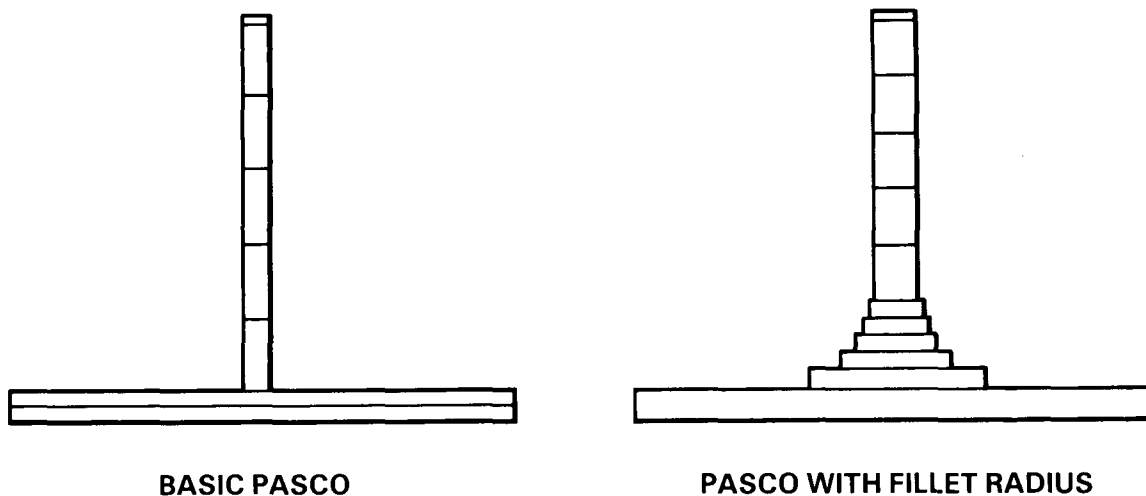

BASIC PASCO   PASCO WITH FILLET RADIUS

Figure 4

17

Two full scale tests were run on the integrally machined waffle panels (ref. 10). For both tests, a series of uniaxial strain gages were used to determine the stress in the expected area of failure. The gages were placed in the pockets and, where applicable, on the base, sides, and tip of the stiffeners. The first test was a study of the pocket buckling allowable for the waffle skin panel. In this test the stiffener was machined so that the skin was critical. The second test was a study of the stiffener buckling allowable. In this test, the stiffener was undercut to make the stiffener critical. The test panels were 19 by 20 inches and 14 by 20 inches, respectively. They were installed on a Tinius Olsen Compression Test Machine, which can deliver up to 440,000 pounds of load. The load was applied in the longitudinal direction. The panels were placed vertically on the test machine. A metal slab sandwiched between the panel ends and the test bed uniformly distributed the compressive load. In order to simulate simply support condition, I-beams were firmly placed, but not clamped, along the longitudinal edges. In both tests the load was increased incrementally by 5,000 pounds to the point of failure with stress readings taken at the end of each interval. The stress readings were tabulated with the corresponding applied loads. Geometry dimensions used in the two tests are shown in figure 5. A picture of the test setup is shown in figure 6.
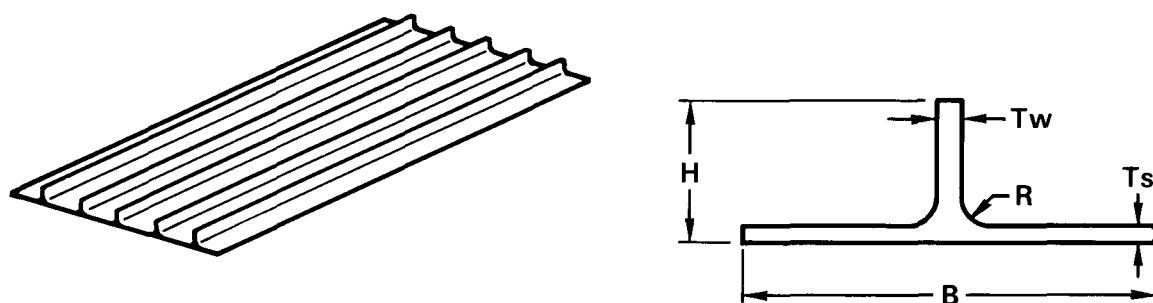
GEOMETRY	TEST 1	TEST 2
B	3.00 IN.	2.24 IN.
H	0.80 IN.	1.13 IN.
Ts	0.066 IN.	0.070 IN.
Tw	0.086 IN.	0.058 IN.
R	0.19 IN.	0.19 IN.
L	4.00 IN.	3.38 IN.
a × b	19 × 20 IN.	14 × 20 IN.

Figure 5

TEST SETUP

Figure 6

19
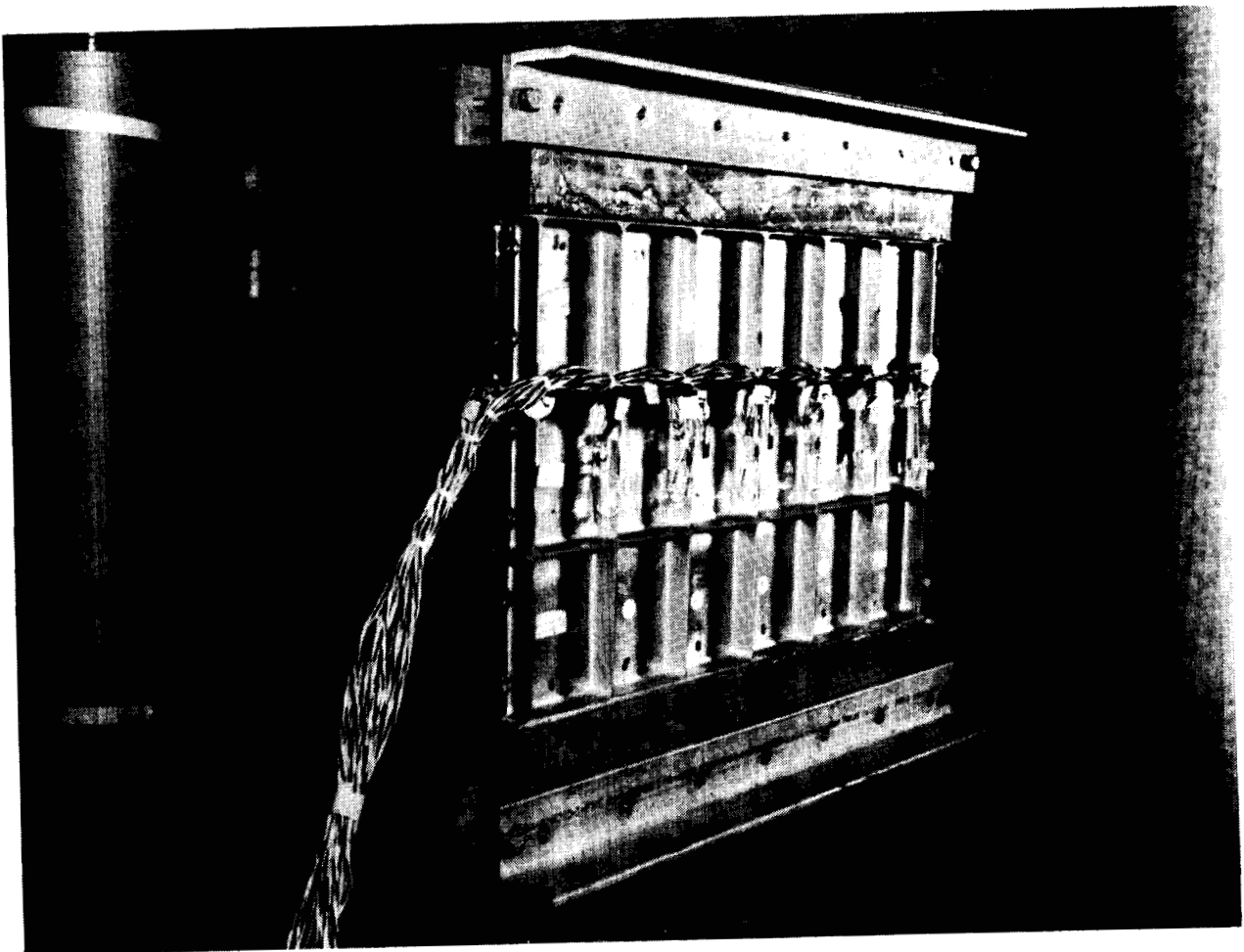
Plots of stress versus longitudinal compressive load are shown in figure 7. The relationship between the applied load and the induced stress is, as expected, very close to linear. Stress readings were taken from the appropriate strain gages mounted in the buckled areas (pocket skin in the first test and the stiffener in the second test). The results of the tests as well as the results predicted by WAFFLE and PASCO are shown in the following chart. The actual test result in each test is the average of the two strain gages.

Method	Test 1 Buckling Half-Wavelength		Test 2 Buckling Half-Wavelength	
	$\lambda = L/2$	$\lambda = L$	$\lambda = L/2$	$\lambda = L$
WAFFLE	N/A	21,121 psi	N/A	15,259 psi
PASCO without fillet	24,492 psi	23,127 psi	26,316 psi	31,205 psi
PASCO with fillet	28,805 psi	33,319 psi	38,067 psi	43,473 psi
Actual test	30,000 psi	N/A	39,750 psi	N/A

FIGURE 7. RESULTS

FIGURE 7. RESULTS (CONT)

Figure 7

REFERENCES

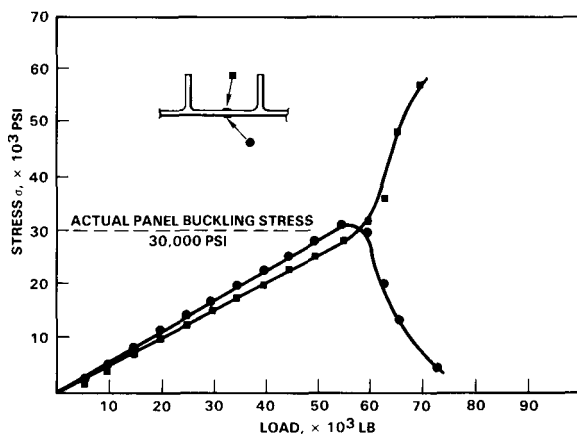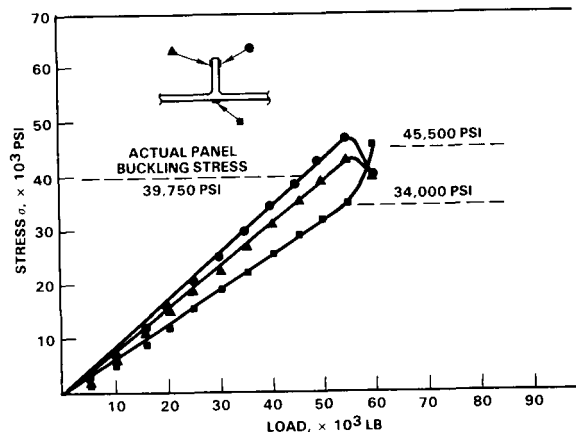1. Gerald, George and Becker, Herbert: Handbook of Structural Stability, Part I, Buckling of Flat Plate. NACA Technical Note 3781, July 1957.

2. Becker, Herbert: Handbook of Structural Stability, Part II, Buckling of Composite Elements. NACA Technical Note 3782, July 1957.

3. Gerald, George: Handbook of Structural Stability, Part IV, Failure of Plates and Composite Elements. NACA Technical Note 3784, August 1957.

4. Gerald, George: Handbook of Structural Stability, Part V, Compressive Strength of Flat Stiffened Panels. NACA Technical Note 3785, August 1957.

5. Gerald, George and Becker, Herbert: Handbook of Structural Stability, Part VII, Strength of Thin Wing construction. NACA Technical Note D-162, September 1959.

6. Yin, Dah N.: Integrally Machined Panel With Longitudinal and Transverse Stiffeners. WAFFLE Analysis Program (to be published). Rockwell International, Space Transportation Systems Division.

7. Stroud, W. Jefferson and Anderson, Melvin S.: PASCO: Structural Panel Analysis and Sizing Code, Capability and Analytical Foundations, Langley Research Center, Hampton, Virginia. Memorandum 80181, November 1981.

8. Anderson, Melvin S.: Stroud, W. Jefferson; Durling, Barbara J.; and Hennessy, Katherine W. PASCO: Structural Panel Analysis and Sizing Code, User's Manual Langley Research Center, Hampton, Virginia. NASA Technical Memorandum 80182, November 1981.

9. Stroud, W. Jefferson; Greene, William H.; and Anderson, Melvin S.: Buckling Loads of Stiffened Panels Subjected to Combined Longitudinal Compression and Shear: Results Obtained With PASCO, EAL, and STAGS Computer Programs Langley Research Center, Hampton, Virginia. NASA Technical Paper 2215, 1984.

10. Local Stiffener and Skin Pocket Buckling of Integrally Machined Stiffened Panel Test Report. Rockwell International, Space Transportation Systems Division, December 1980.

11. Timoshenko, Stephen P. and Gere, James M.: Theory of Elastic Stability. McGraw-Hill Book Company, Inc. Second Edition, 1961.

12. Dow, Norris F.; Libove, Charles; and Hubka, Ralph E.: Formulas for Elastic Constants of Plates With Integral Waffle-Like Stiffening. NACA Report 1195, 1954.

MODELING THE MISSILE-LAUNCH TUBE
PROBLEM IN DYSCO

Alex Berman
Bruce A. Gustavson
Kaman Aerospace Corporation
Bloomfield, Connecticut

INTRODUCTION

DYSCO is a versatile, general purpose dynamic analysis program which assembles equations and solves dynamics problems. The "executive" manages a library of technology modules which contain routines that compute the matrix coefficients of the second order ordinary differential equations of the components. The executive performs the coupling of the equations of the components and manages the solution of the coupled equations.

Any new component representation may be added to the library if, given the state vector, one can write a FORTRAN program to compute M, C, K, F. The problem described in this report demonstrates the generality of this statement.

o   DYSCO - MODELS AND SOLVES DYNAMIC SYSTEMS

o   EXECUTIVE MANAGES A LIBRARY OF TECHNOLOGY MODULES

o   TECHNOLOGY MODULES DEFINE SECOND ORDER ODE (M, C, K, F)

o   EXECUTIVE COUPLES COMPONENTS AND MANAGES SOLUTIONS

o   NEW MODULES MAY BE ADDED TO LIBRARY IF:

        GIVEN THE STATE OF THE COMPONENT, A
        FORTRAN PROGRAM CAN COMPUTE M, C, K, F

Figure 1

Consider an elastic body (missile) moving through an elastic tube. The inside of the tube is populated with snubbers having spring and damper characteristics with gaps between the missile and the snubbers.

The complete problem also must include aerodynamic effects, control devices and algorithms, and propulsive force history. All of these are readily treated in DYSCO.

The emphasis of this presentation will be the treatment of time varying constraints.
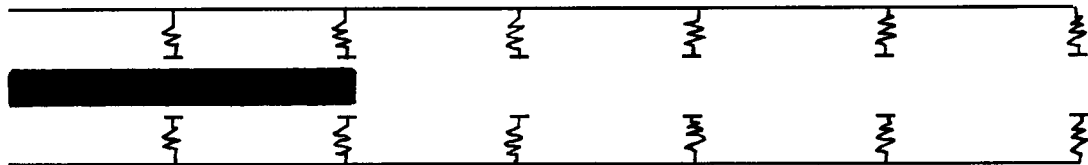
CHARACTERISTICS

    MISSILE AND TUBE ARE ELASTIC BODIES
    GAPS EXIST BETWEEN MISSILE AND SNUBBERS
    AERODYNAMIC EFFECTS, CONTROLS, PROPULSIVE FORCE MUST BE
       CONSIDERED

BASIC PROBLEM IS TIME VARYING CONSTRAINTS

Figure 2

The component illustrated in Figure 3a was added to the technology library. The "MS" stands for "moving structure." Note that there are no dynamic characteristics associated with the degrees of freedom in this component. The names of the DOF Z_1, ... Z_N are arbitrary and supplied by the user. When these correspond to those of another component, DYSCO automatically performs the dynamic coupling. The same is true of the DOF Z_L and Z_U.

Figure 3b illustrates a particular state of the system and illustrates how the force vector is coupled (M, C, K are treated as null). In this illustration, forces act only on DOF Z4, Z5, and ZU. All other forces are zero.
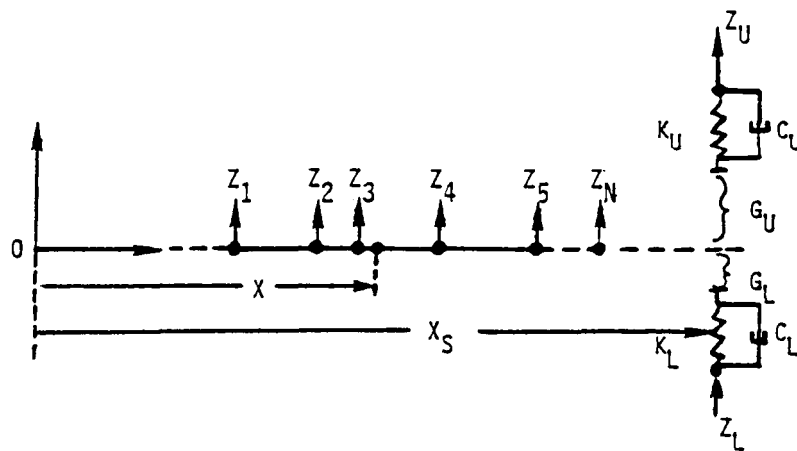
Figure 3a

Figure 3b

26
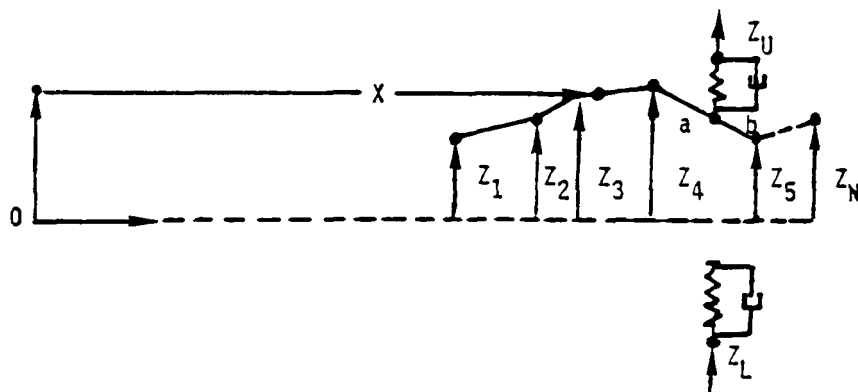
MISSILE-LAUNCH TUBE MODEL

The figure illustrates the DYSCO model used to represent this problem. The missile and the tube are represented by modal representations (CFM2), six snubbers as previously described (CMS1) are used, each identified by the tube station at which it is located.
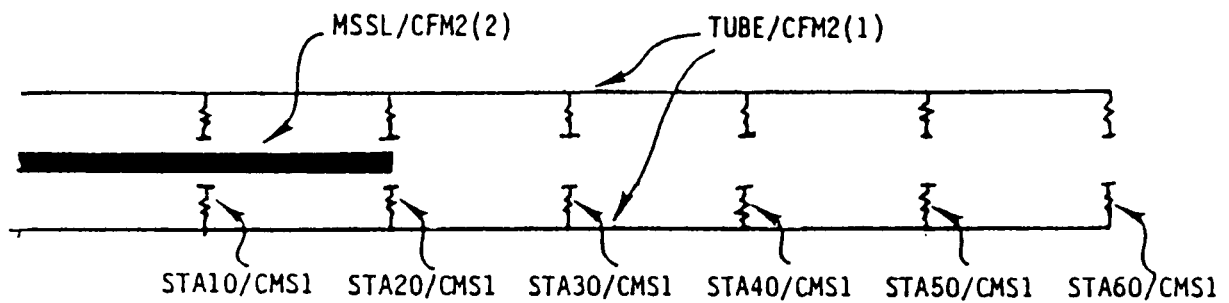

```
************************         MODEL MT         **************************

BASIC MISSILE IN TUBE

INDEX     COMP     NO.     DATA SET          FORCE          DATA SET

  1       CFM2      1      TUBE              NONE
  2       CFM2      2      MSSL              NONE
  3       CMS1             STA10             NONE
  4       CMS1             STA20             NONE
  5       CMS1             STA30             NONE
  6       CMS1             STA40             NONE
  7       CMS1             STA50             NONE
  8       CMS1             STA60             NONE
**************************************************************************
```

Figure 4

This set of data defines the tube used in the sample analysis. Note the DOF names shown are also used on the snubber springs and dampers and are thus automatically attached to the tube at the proper station.

```
        ZL10      ZL20      ZL30      ZL40      ZL50      ZL60
          ▲         ▲         ▲         ▲         ▲         ▲
          |         |         |         |         |         |
  _____|_____|_____|_____|_____|_____|
  0      10"       20"       30"       40"       50"       60"
```
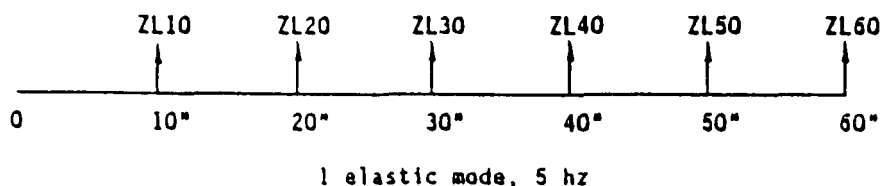
1 elastic mode, 5 hz

```
** '*************************      TUBE / CFM2    ***************************
MISSILE LAUNCHER - NO X DOF. COMP 1.
***********************************************************************************
INPUT FOR STRUCTURAL     COMPONENT CFM2. MODAL FUSELAGE
    1 RBM      - RIGID BODY MODES     •       NO
    2 NMOD     - NO. OF ELASTIC MODES •        1
    3 NS       - NO. FUSELAGE STAS    •        6
    4 X        - (REAL) INPUT STATION VALUES
                -2.00000E+01   -1.00000E+01   0.00000E+00   1.00000E+01
                 2.00000E+01    3.00000E+01
    5 VC1      - MODE1 VERTICAL COMP   •      YES
    6 Z1       - (REAL) MODE1 VERTICAL DISP
                 2.00000E-01   -4.00000E-01  -6.00000E-01  -4.00000E-01
                 2.00000E-01    1.00000E+00
    7 ZP1      - (REAL) MODE1 VERTICAL SLOPE
                 0.00000E+00    0.00000E+00   0.00000E+00   0.00000E+00
                 0.00000E+00    0.00000E+00
    8 LC1      - MODE1 LATERAL COMP    •       NO
    9 TC1      - MODE1 TORSION COMP    •       NO
   10 NR       - NO. OF ROTORS         •        0
   11 NI       - NO. OTHER IMPLCT DOF  •        6
   12 CIDFL    - (DOF) IMPLICIT DOF NAMES
             ZL10   0   ZL20   0   ZL30   0   ZL40   0   ZL50   0
             ZL60   0
   13 XSTA     - (REAL) STAS FOR IMPLCT DOF
                -2.00000E+01   -1.00000E+01   0.00000E+01   1.00000E+01
                 2.00000E+01    3.00000E+01
   14 AF       - (REAL) FWD ANGLE FROM VERT
                 0.00000E+00    0.00000E+00   0.00000E+00   0.00000E+00
                 0.00000E+00    0.00000E+00
   15 AL       - (REAL) LAT ANGLE FROM VERT
                 0.00000E+00    0.00000E+00   0.00000E+00   0.00000E+00
                 0.00000E+00    0.00000E+00
   16 MMS      - MODAL MASS (SLUGS)   • 2.00000E+00
   17 MD       - MODAL DAMPING (PC1)  • 0.00000E+00
   18 FREQ     - MODAL FREQUENCY (HZ) • 5.00000E+00
```
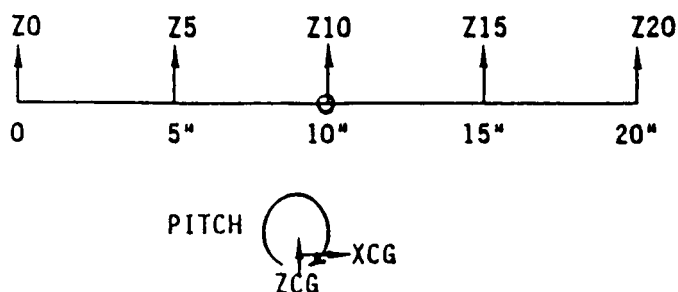
Figure 5

MISSILE DATA SET

This set of data defines the missile used in the sample analysis. Note the DOF names which are used in the new component.


```
**************************** MSSL /CFM2 ****************************
MISSILE - X DOF. COMP 2.
*******************************************************************
INPUT FOR STRUCTURAL     COMPONENT CFM2. MODAL FUSELAGE
    1 RBM      - RIGID BODY MODES     =        YES
    2 IXCG     - LONGITUDINAL         =        YES
    3 IYCG     - LATERAL              =        NO
    4 IZCG     - VERTICAL             =        YES
    5 IROLL    - ROLL                 =        NO
    6 IPTCH    - PITCH                =        YES
    7 IYAW     - YAW                  =        NO

    8 CG       - CG STATION (IN)      = 0.00000E+00
    9 NMODE    - NO. OF ELASTIC MODES =        0
   10 NR       - NO. OF ROTORS        =        0
   11 NI       - NO. OTHER IMPLCT DOF =        5
   12 CIDFL    - (DOF) IMPLICIT DOF NAMES
              Z0   0   Z5   0   Z10   0   Z15   0   Z20   0
   13 XSTA      - (REAL) STAS FOR IMPLCT DOF
              -1.00000E+01   -5.00000E+00   0.00000E+00   5.00000E+00
               1.00000E+01
   14 AF        - (REAL) FWD ANGLE FROM VERT
               0.00000E+00   0.00000E+00   0.00000E+00   0.00000E+00
               0.00000E+00   0.00000E+00
   15 AL        - (REAL) LAT ANGLE FROM VERT
               0.00000E+00   0.00000E+00   0.00000E+00   0.00000E+00
               0.00000E+00   0.00000E+00
   16 MASSL     - FUSELAGE MASS (LB)   = 5.00000E+00
   17 IMYF      - PITCH MOI ABOUT CG   = 4.00000E-02
```
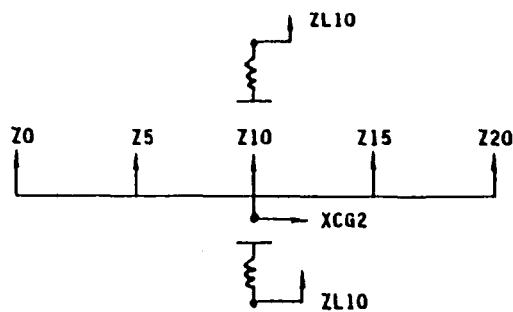
Figure 6

STA 10 SNUBBER DATA SET

Note the relationship between the DOF and those of the missile and the tube on previous figures.


```
**************************         STA10/CHS1        **************************
TUBE SNUBBER, STA 10
*****************************************************************************
INPUT FOR STRUCTURAL    COMPONENT CFM2. MODAL FUSELAGE
    1 IU       - UPPER BASE DOF        =      YES
    2 CDFLU    - UPPER BASE DOF NAME   =    ZL10   0
    3 KU       - UPPER SPRING COEFF    = 2.00000E+02
    4 CU       - UPPER DAMPER COEFF    = 0.00000E+00
    5 GU       - UPPER GAP             = 5.00000E-01
    6 IL       - LOWER BASE DOF        =      YES
    7 CDFLL    - LOWER BASE DOF NAME   =    ZL10   0

    8 KL       - LOWER SPRING COEFF    = 2.00000E+02
    9 CL       - LOWER DAMPER COEFF    = 0.00000E+00
   10 GL       - LOWER GAP             = 5.00000E-01
   11 CDFLX    - HORIZONTAL DOF NAME   =   XCG 2000
   12 XS       - BASE DISTANCE         = 0.00000E+00
   13 NCDFZ    - NO. OF VERTICAL DOF   =       5
   14 CDFLZ    - (DOF) VERTICAL DOF NAMES
           Z0   0   Z5   0   Z10   0   Z15   0   Z20   0
   15 XZ       - (REAL) VERT DOF STATIONS
           -1.00000E+01  -5.00000E+00   0.00000E+00   5.00000E+00
            1.00000E+01
```
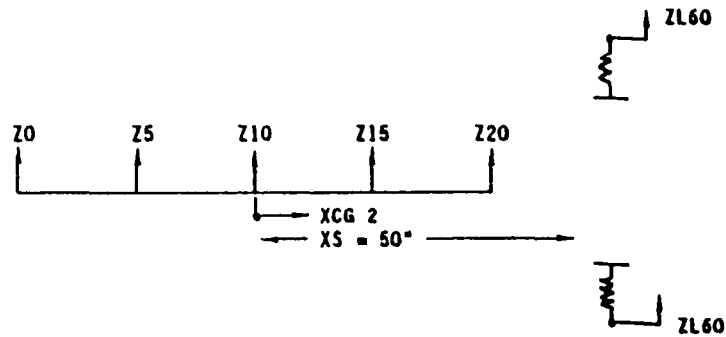
Figure 7

STA 60 SNUBBER DATA SET

Note DOF names on this data set and how they relate to missile and tube data.


```
****************************      STA60/CHS1      ****************************
TUBE SNUBBER, STA 60
********************************************************************************
INPUT FOR COMPONENT CHS1. MOVING CONSTRAINTS
    1 IU         - UPPER BASE DOF      =        YES
    2 CDFLU      - UPPER BASE DOF NAME =     ZL60   0
    3 KU         - UPPER SPRING COEFF  = 2.00000E+02
    4 CU         - UPPER DAMPER COEFF  = 0.00000E+00
    5 GU         - UPPER GAP           = 5.00000E-01
    6 IL         - LOWER BASE DOF      =        YES
    7 CDFLL      - LOWER BASE DOF NAME =     ZL60   0

    8 KL         - LOWER SPRING COEFF  =   2.00000E+02
    9 CL         - LOWER DAMPER COEFF  =   0.00000E+00
   10 GL         - LOWER GAP           =   5.00000E-01
   11 CDFLX      - HORIZONTAL DOF NAME =     XCG 2000
   12 XS         - BASE DISTANCE       =   5.00000E+01
   13 NCDFZ      - NO. OF VERTICAL DOF =         5
   14 CDFLZ      - (DOF) VERTICAL DOF NAMES
            ZO   0   ZS   0   Z10   0   Z15   0   Z20   0
   15 XZ         - (REAL) VERT DOF STATIONS
            -1.00000E+01  -5.00000E+00   0.00000E+00   5.00000E+00
             1.00000E+01
```

Figure 8

TIME HISTORY

This figure illustrates a sample time history of the missile with and without damping in the snubbers.

The procedure is shown to perform as planned.

Future enhancements could include more general shape functions, nonlinear springs, friction forces.
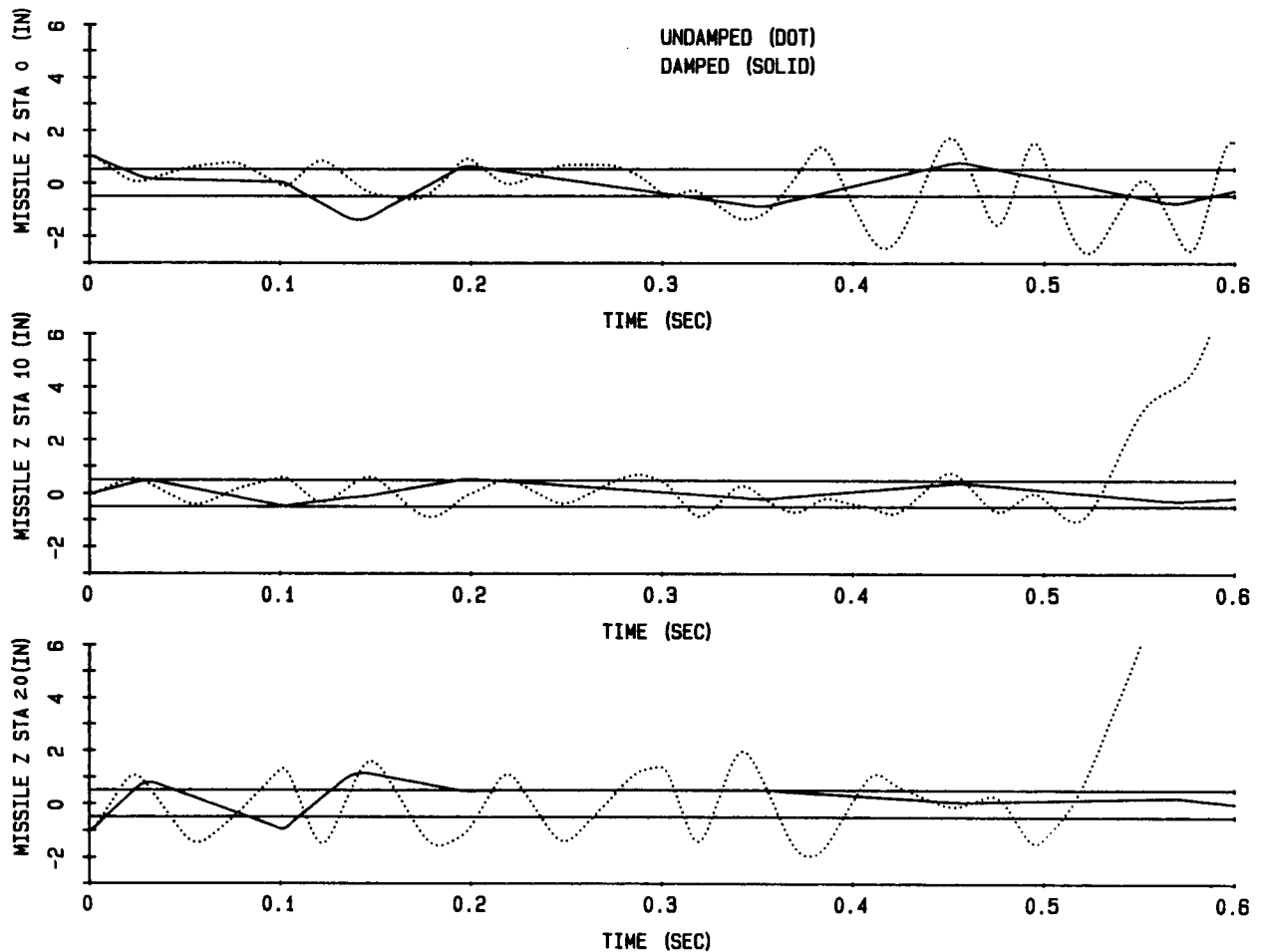

Figure 9

SESSION 53 - WORK-IN-PROGRESS II

Influence of Time Lag and Noncolocation on Integrated Structural/Control System Designs[†]

R. A. Manning[*] and L. A. Schmit[**]

[*] Member of the Technical Staff,
   TRW Space and Technology Group
[**] Professor of Engineering and Applied Science,
   University of California, Los Angeles

Introduction

Recent research efforts have led to the development of simultaneous structural/control system design procedures [1 − 3]. Absent in any of this work is the time delay present in the control system sensors and actuators and the computational time delay for synthesizing actuator commands from sensor measurements. Madden [4] has shown that the time delay present in the control system can have profound effects on the resulting system performance and stability regardless of its source. In addition, many of the simultaneous structural/control system design procedures have used colocated sensors and actuators for implementation of the control system. In actual practice, colocation is not always possible (e.g., actuator output forces are based on optical quality measurements such as line-of-sight). Spector and Flashner [5] and Bong Wei [6] have raised the issue of stability degradation when using noncolocated sensor and actuators.

This work extends the integrated structural/control system design procedure reported in Reference [3] to include the effects of time lag and noncolocation of sensors and actuators on the resulting optimum designs.

Optimum Design Problem Statement

In Reference [3] the integrated controls/structure optimum design problem was posed as either the mass minimization problem given in equations (1) through (4) or the control effort minimization problem given in equations (5) through (8). The set of behavior constraints, $g_m(d,t)$, consists of time parametric upper bounds on the peak transient dynamic displacements and accelerations at selected degrees-of-freedom as well as upper or lower bounds on selected natural frequencies. The vector of design variables, d, consists of finite element box beam cross-sectional dimensions, spherical nonstructural mass element radii, and nonlinear on/off control system velocity thresholds and actuator output force magnitudes.

The solution to either the mass minimization problem or the control effort minimization problem is found by solving a sequence of explicit approximate problems. Each approximate problem is constructed using first order hybrid approximations for all of the critical (or near critical) behavior constraints as well as for the control effort objective function in (5) or upper bound constraint in (3). Time parametric peak transient dynamic displacement and/or acceleration sensitivities for use in the hybrid approximations are calculated in an efficient manner using the Wilkie-Perkins essential parameter sensitivity method [7, 8] which significantly reduces the amount of time stepping needed to obtain these sensitivities.

$$\min W(d) \tag{1}$$

$$\text{subject to } g_m(d,t) \geq 0 \tag{2}$$

$$E(d,t_f) \leq E^u \tag{3}$$

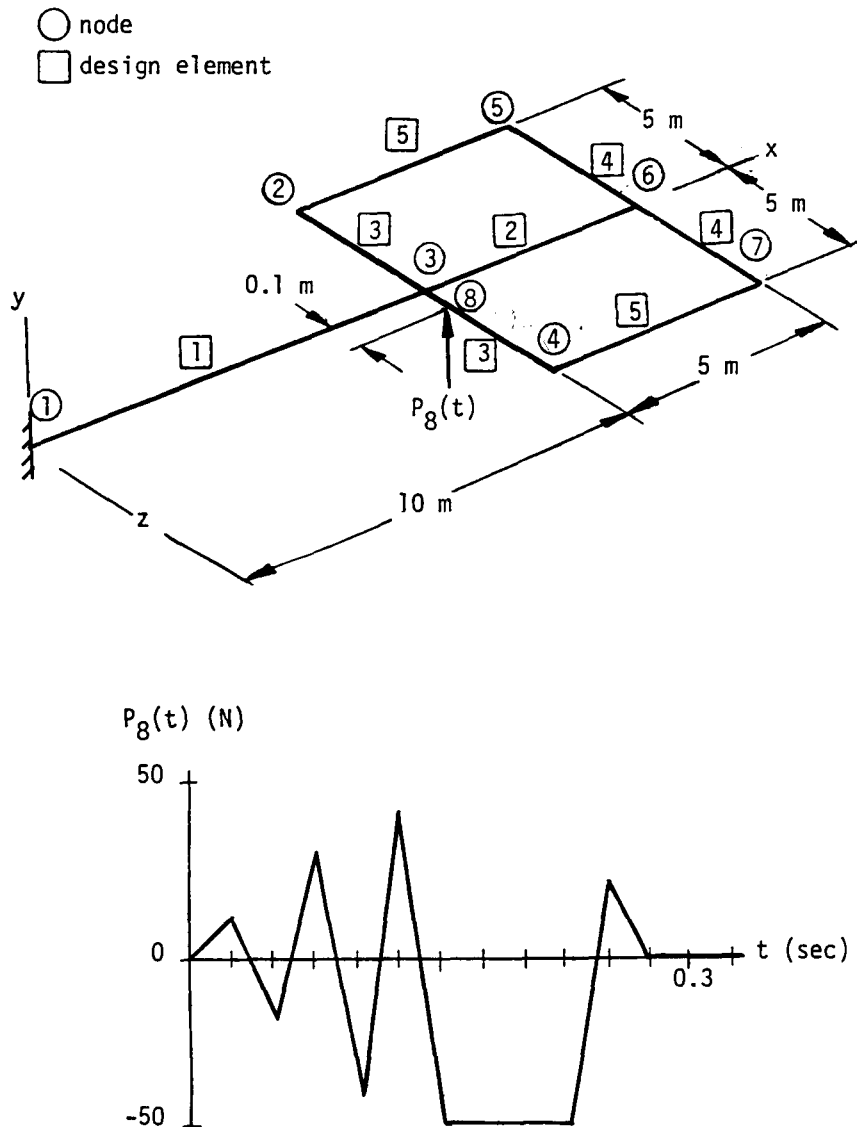$$d_j{}^l \leq d_j \leq d_j{}^u \tag{4}$$

or

$$\min E(d,t_f) \tag{5}$$

$$\text{subject to } g_m(d,t) \geq 0 \tag{6}$$

$$W(d) \leq W^u \tag{7}$$

$$d_j{}^l \leq d_j \leq d_j{}^u \tag{8}$$

Numerical Example

The 21 degree-of-freedom aluminum grillage structure shown is used to examine the effects of control system delay and noncolocation of sensors and actuators on the resulting optimum designs. Nine analysis box beam finite elements are linked to yield five design elements. The external load shown was applied at node 8 of the structure so as to excite both cantilever bending modes and torsional modes. A colocated sensor/actuator pair is located at node 6 of the structure to try and reduce dynamic response. Upper bounds of 9.0×10^{-4}m were placed on the peak dynamic displacement response at nodes 5, 6, and 7. All dynamic response calculations were carried out for 1 second using 10 retained modes (frequency content up to 100 Hz), 2% modal damping, and a time step of 0.005 seconds. Both the minimum weight problem (with an upper bound placed on control effort) and the minimum control effort problem (with a weight cap) were used to demonstrate the effects of control system time lag on the resulting optimum designs. Results for this problem were reported in Reference [3] using colocated sensors and actuators and no time lag.

The actuator output forces were represented as exponential growth functions with the value of the time lag defined as the time it takes to generate 90% of the maximum actuator output force from the time the actuator is commanded to generate force. For each value of time lag, a complete optimization was done from the same starting point. The results of the optimizations for each time lag are shown in the accompanying tables and figures.
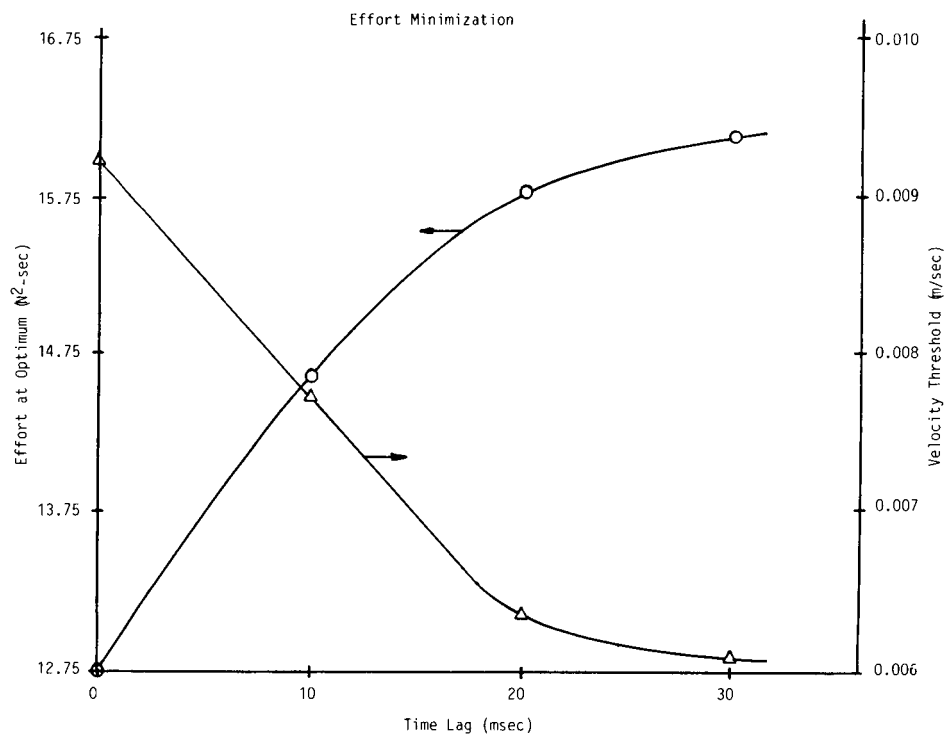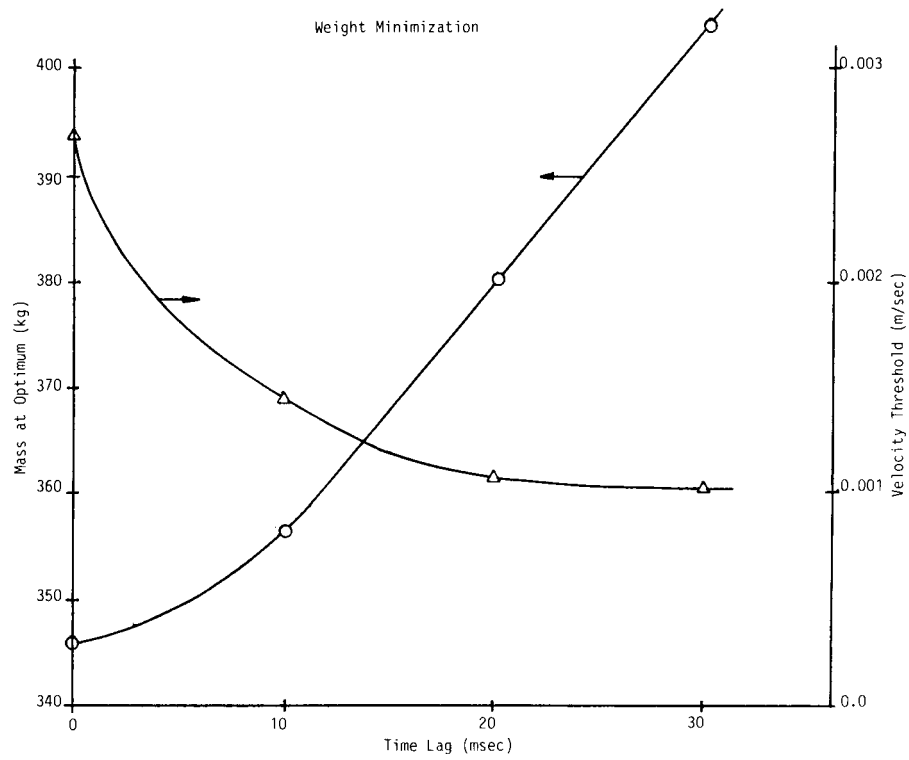
The figures show that the value of the objective function increases with increasing time lag when displacement constraints drive the optimum design. Also plotted in the figures are the corresponding values of the velocity threshold design variable, ϵ_i. One can see that as the time lag increases, the value of the velocity threshold at the optimum design decreases. This indicates that the optimizer is compensating for the time lag by commanding the actuators to generate force sooner. At time lag values greater than 15 milliseconds the minimum weight increases nearly linearly since the velocity threshold design variable is against its lower bound side constraint.

Time histories for the critical constraints and corresponding actuator forces are shown on the following pages.
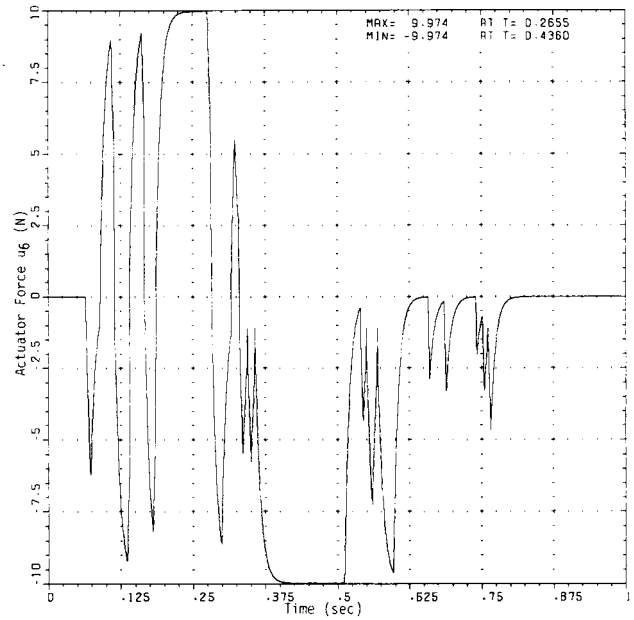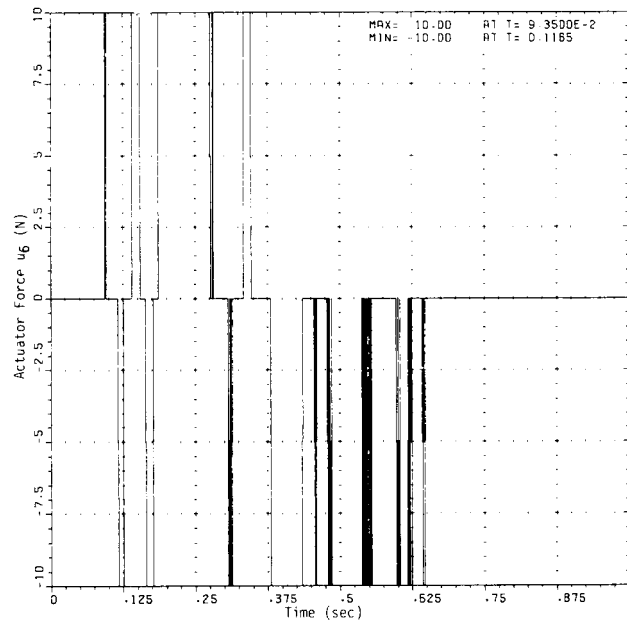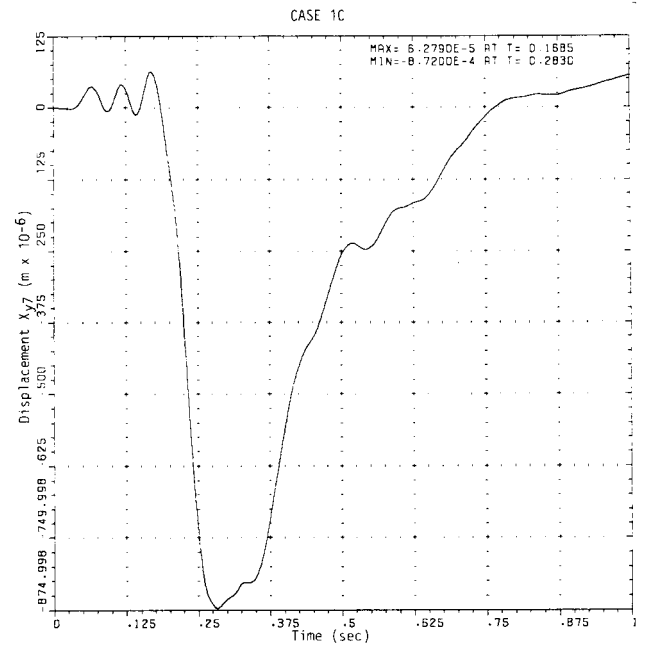
Table 1: Effect of Time Lag on the Optimum Designs

Case	Objective Function	Time Lag (sec)	Objective Function Value	Critical Behavior Constraints
1A	mass	0.0001	346	X_{y7}
1B	mass	0.0010	357	X_{y7}
1C	mass	0.0020	381	X_{y7}
1D	mass	0.0030	404	X_{y7}
2A	effort	0.0001	12.75	X_{y6}, X_{y7}, W
2B	effort	0.0010	14.65	X_{y6}, X_{y7}, W
2C	effort	0.0020	15.85	X_{y6}, X_{y7}, W
2D	effort	0.0030	16.15	X_{y6}, X_{y7}, W

Numerical Results - With Time Lag
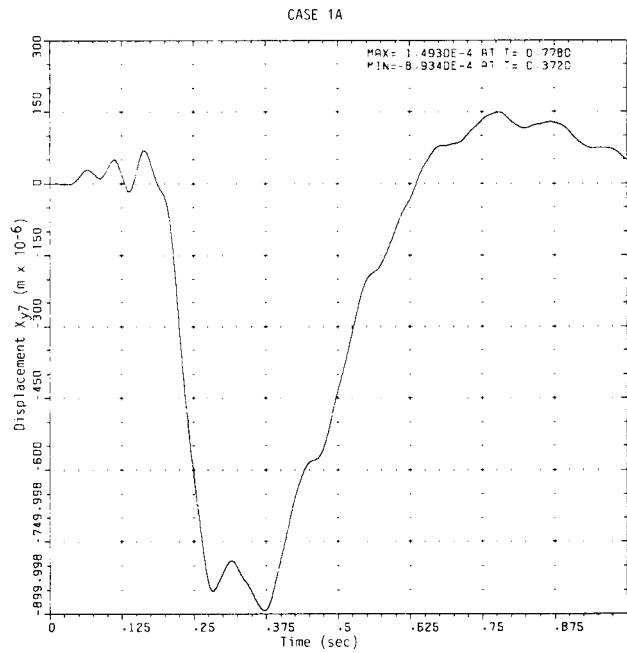
Weight Minimization

Effort Minimization

CASE 1A

CASE 1C

Numerical Results - With Time Lag

CASE 2A

MAX= 6.9940E-4 AT T= 0.5145
MIN=-9.0850E-4 AT T= 0.2985

CASE 2C

MAX= 4.2690E-4 AT T= 0.6190
MIN=-8.7900E-4 AT T= 0.2935

MAX= 10.00 AT T= 0.1955
MIN= -10.00 AT T= 0.3880

MAX= 9.950 AT T= 0.2670
MIN= -9.671 AT T= 0.4045

41
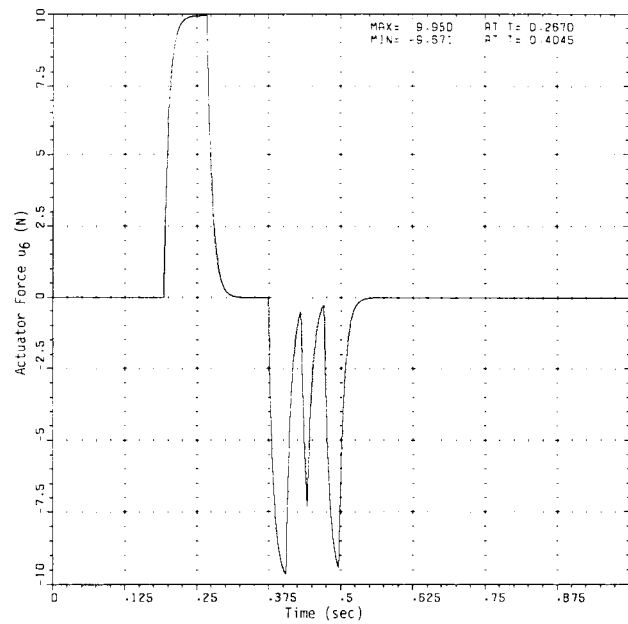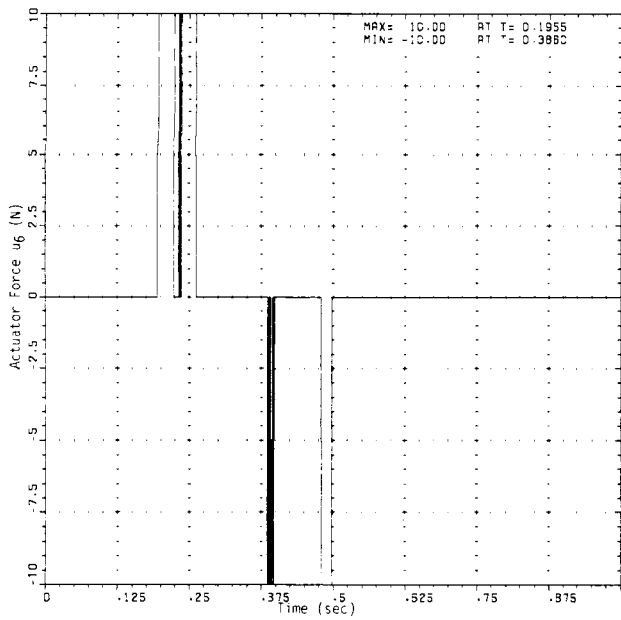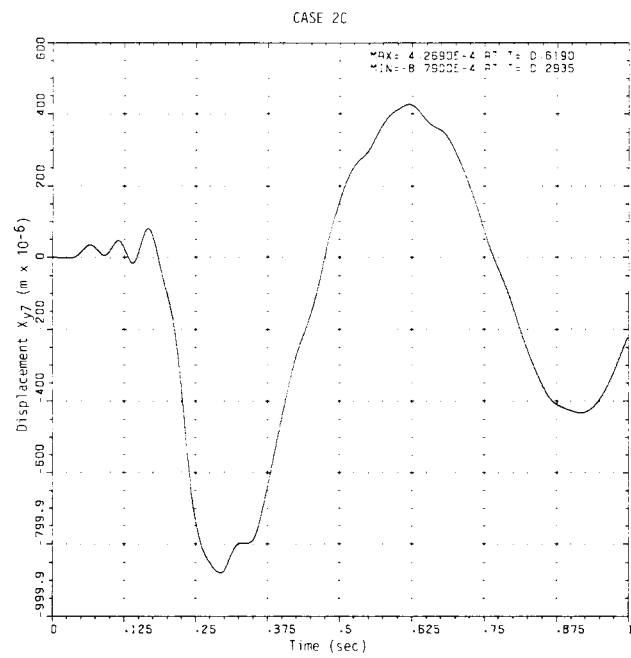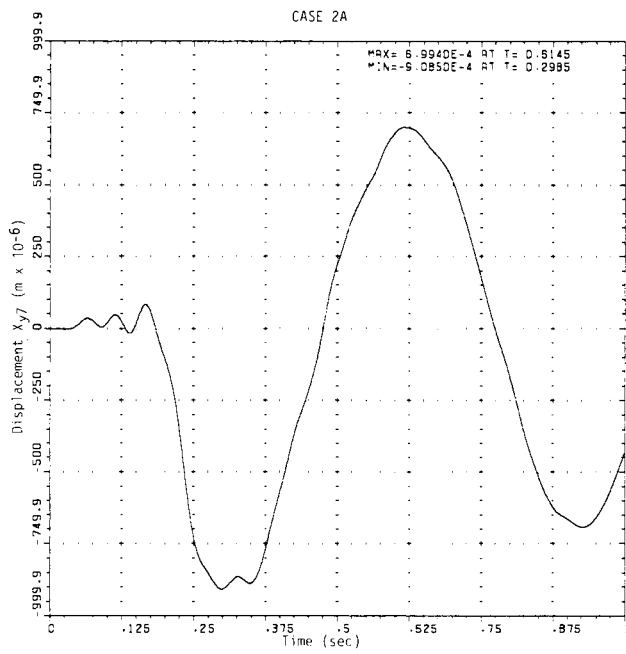
Numerical Results - Noncolocated Sensors and Actuators

The minimum weight design problem was run again using noncolocated sensors and actuators without time lag. In this case, simple estimators (based on kinematics) had to be constructed to generate velocities at actuators locations from the measured velocities at sensor locations. Case 3A in the table below gives the result obtained in Reference [3] for colocated sensors and actuators. The two configurations of noncolocated sensor/actuator locations, their respective estimators, and the resulting optimum designs are given in the table as cases 3B and 3C.

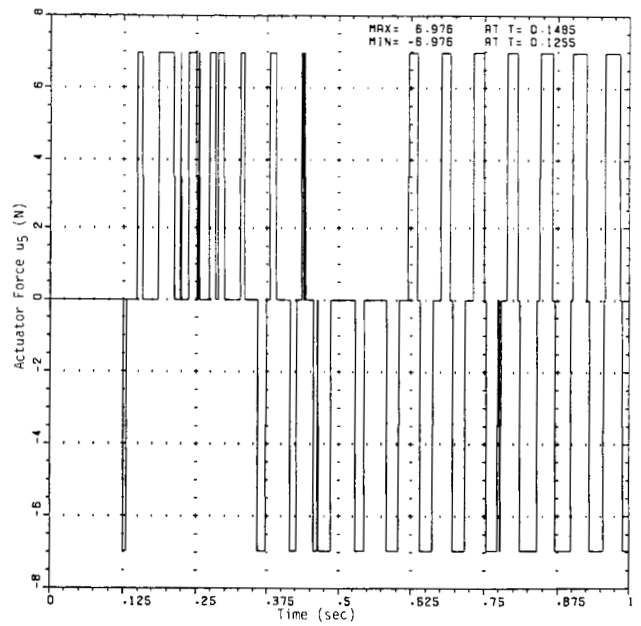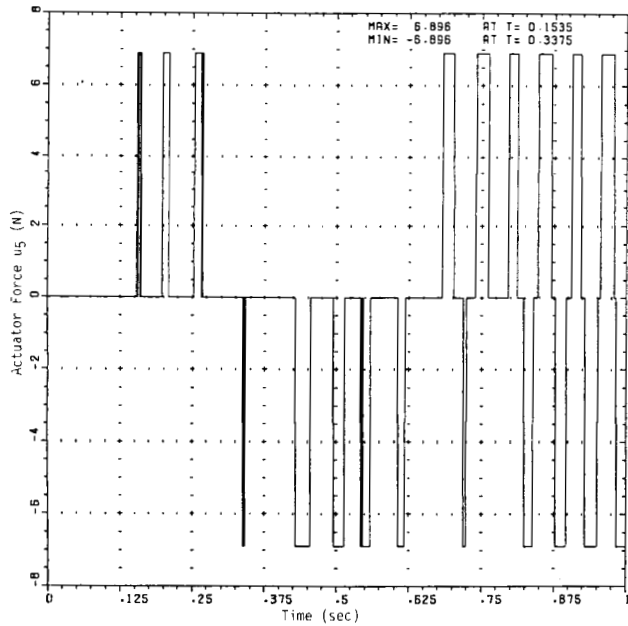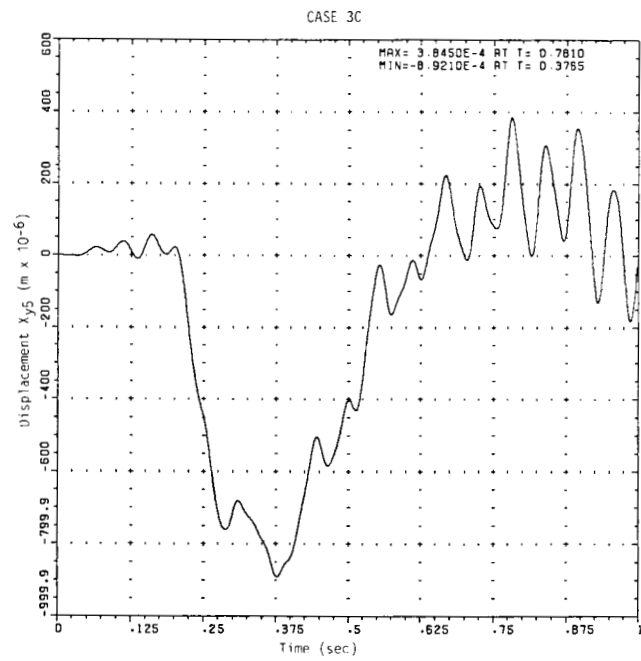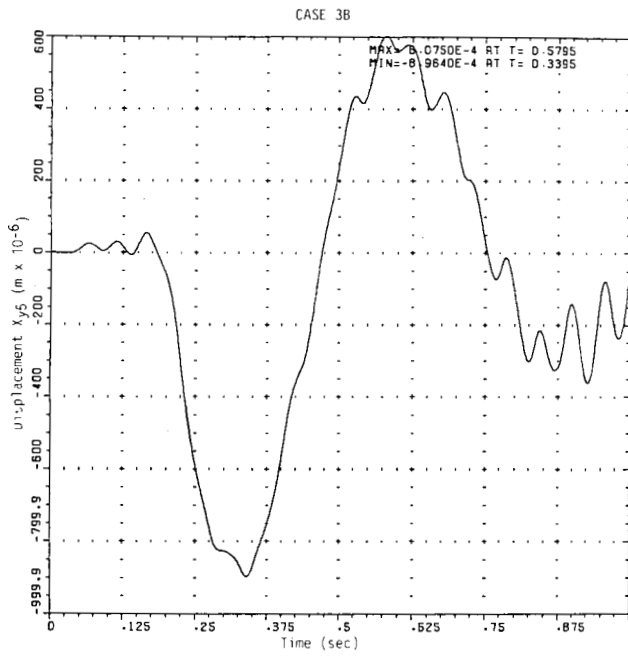Case 3B and 3C time histories for the critical constraint at the optimum designs, X_{y5}, along with the actuator force outputs are shown in the accompanying figures. In both instances, peak dynamic displacements are reduced in the time period considered when compared with the uncontrolled case. However, towards the end of the time history, both cases show high frequency oscillations superimposed on the response. In fact, both responses are unstable if carried out for a longer period of time. This instability is caused entirely by the fifth mode (17.8 Hz in case 3B, 18.2 Hz in case 3C) where the sign of the translational component of the eigenvector at the sensor location is opposite to the sign at the actuator locations. As pointed out by Bong Wie [6], systems with noncolocated sensors and actuators tend to be closer to the stability bounds for just that reason. The actuator force time histories show that the control system is pumping energy into the system at exactly the frequency of the fifth mode, thus driving it unstable.

Table 2: Effect of Noncolocation on the Optimum Designs

Case	Nodal Sensor Locations	Nodal Actuator Locations	Estimator Equations	Objective Function Values
3A	5,7	5,7		259
3B	6	5,7	$X_{y5} = X_{y6} + 5X_{\theta_x 6}$ $X_{y7} = X_{y6} - 5X_{\theta_x 6}$	406
3C	3	5,7	$X_{y5} = X_{y3} + 5X_{\theta_x 3} + 5X_{\theta_z 3}$ $X_{y7} = X_{y3} - 5X_{\theta_x 3} + 5X_{\theta_z 3}$	423

Numerical Results - Noncolocated Sensors and Actuators

CASE 3B

MAX= 3.075DE-4 AT T= 0.5795
MIN=-8.9640E-4 AT T= 0.3395

CASE 3C

MAX= 3.845DE-4 AT T= 0.7810
MIN=-8.9210E-4 AT T= 0.3765

MAX= 6.896 AT T= 0.1535
MIN= -6.896 AT T= 0.3375

MAX= 6.976 AT T= 0.1485
MIN= -6.976 AT T= 0.1255

Concluding Remarks

The effects of including time lag and allowing noncolocated sensors and actuators on optimum designs has been explored. Results of this study show that neglect of time lag in the control system can lead to unconservative designs (i.e., lower objective function designs than can be physically realized). However, the time lag results indicate that it is feasible to incorporate this refinement within a design optimization procedure which includes direct constraints on peak transient dynamic displacements at specified degrees of freedom. Furthermore, it is found that the optimization procedure compensates for the presence of time lag in the system by lowering the velocity thresholds, thus turning on the control system sooner. On the other hand, the use of noncolocated sensors and actuators can result in convergence to a dynamically unstable system when trying to control modes where the sensors and actuators are out of phase with respect to one another. The results for the noncolocated sensors and actuators indicate that it will be necessary to add constraints on appropriate dynamic stability measures in order to prevent unstable behavior.

References

[1] Junkins, J.L., Bodden, D.S., and Turner, J.D., "A Unified Approach to Structure and Control System Design Iterations", presented at the Fourth International Conference on Applied Numerical Modeling, Tainan, Taiwan, December, 1984.

[2] Lust, R.V. and Schmit, L.A., "Control-Augmented Structural Synthesis", *AIAA Journal*, Vol. 26, No. 1, January 1988, pp. 86-95.

[3] Manning, R.A. and Schmit, L.A., "Control Augmented Structural Synthesis with Transient Response Constraints", AIAA Paper No. 87-0749, presented at the 28th AIAA/ASME/ASCE/AHS Structures, Structural Dynamics, and Materials Conference, Monterey, California, April 6-8, 1987, pp. 194-204.

[4] Madden, P., "Slewing and Vibration Suppression for Flexible Structures", presented at the 2nd NASA/DOD Control/Structures Interaction Technology Conference, Colorado Springs, Colorado, November 17-19, 1987, pp. 353-363.

[5] Spector, V.A. and Flashner, H., "Modeling of Non-Collocated Structural Control Systems", AIAA Paper No. 88-4060-CP, presented at the 29th AIAA/ASME/ASCE/AHS Structures, Structural Dynamics, and Materials Conference, Williamsburg, Virginia, April 14-17, 1988, pp. 74-83.

[6] Bong Wie, "Active Vibration Control Synthesis for the Control of Flexible Structures Mast Flight System", *Journal of Guidance, Control, and Dynamics*, Vol. 11, No. 3, May-June 1988, pp. 271-277.

[7] Wilkie, D.F. and Perkins, W.R., "Essential Parameters in Sensitivity Analysis", *Automatica*, Vol. 5, 1969, pp. 191-197.

[8] Manning, R.A., Lust, R.V., and Schmit, L.A., "Behavior Sensitivities for Control Augmented Structures", presented at the Sensitivity Analysis in Engineering Conference, Hampton, Virginia, September 25-26, 1986, NASA CP 2457, pp. 33-57.

INTEGRATED OPTIMIZATION OF NONLINEAR R/C FRAMES
WITH RELIABILITY CONSTRAINTS

Alfredo Soeiro
Dept. of Civil Engineering, Univ. Florida
Gainesville, Florida

Marc Hoit
Dept. of Civil Engineering, Univ. Florida
Gainesville, Florida

Summary

A structural optimization algorithm was researched including global displacements as decision variables. The algorithm was applied to planar reinforced concrete frames with nonlinear material behavior submitted to static loading. The flexural performance of the elements was evaluated as a function of the actual stress-strain diagrams of the materials. Formation of rotational hinges with strain hardening were allowed and the equilibrium constraints were updated accordingly. The adequacy of the frames was guaranteed by imposing as constraints required reliability indices for the members, maximum global displacements for the structure and a maximum system probability of failure.

Previous Research

Structural frame optimization problems have been usually formulated based on the cycling between two distinct phases: analysis and optimal design. The option described in this work combines both phases by the addition of the global displacements to the set of design variables, option researched by several authors (ref. 1 and 2). The main purpose of this strategy was to determine the benefits of extending the linear static formulation to nonlinear static structural problems using the secant stiffness method. The reason behind this research was the fact that the global stiffness changes created by the nonlinear behavior would be considered simultaneously with the changes of the element sizes, thus improving convergence.

The first step of the research was to optimize elastic plane frames with elements with rectangular sections submitted to static loading. The objective function was the volume of the structure and constraints of the optimization problem were equalities representing global equilibrium of the structure and inequalities for the limits on global displacements and the maximum flexural stresses. The strategy adopted consisted of transforming the constrained problem in an unconstrained one using the method of the Augmented Lagrangian Multipliers (ref. 3). The unconstrained minimization was solved using the Hooke and Jeeves method.
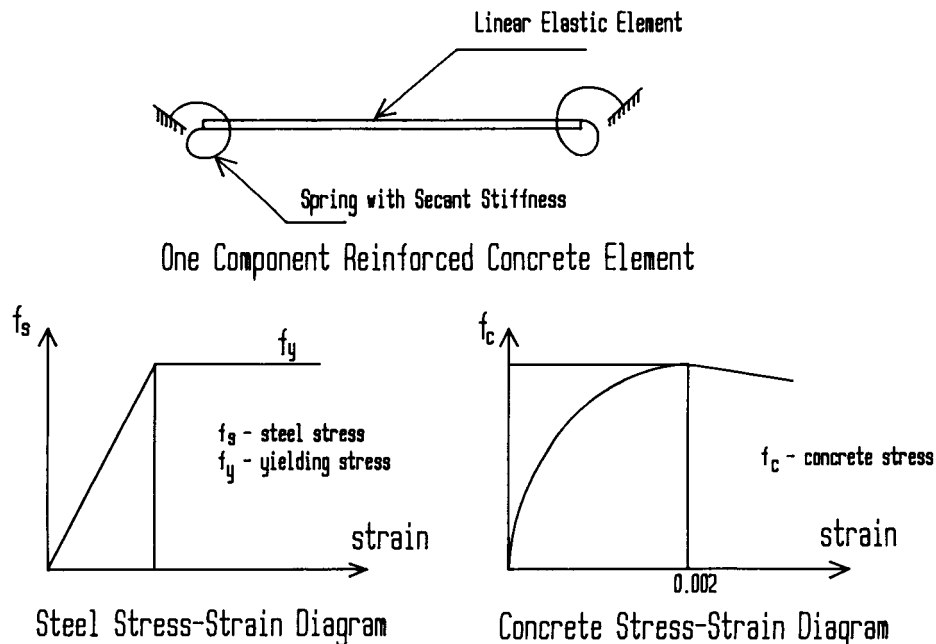
The results with this formulation were encouraging and the optimal solutions were found. The convergence rate was dependent on the initial design, scaling, penalty parameters and lagrangian multipliers values. The computational effort was considerable when compared with other explored techniques based on optimality criteria and mathematical programming methods. To improve the efficiency of the algorithm a gradient technique was implemented to solve the unconstrained minimization problem. This improvement was unsuccessful since the Augmented Lagrangian function was very steep, with large sensitivity to any small variation of the displacement variables.

Nonlinear Formulation

The following logical objective was to extend this strategy to nonlinear reinforced concrete frames. The typical frame element has rectangular cross section and is doubly reinforced with equal amount of flexural steel on both sides. The model adopted for the inelastic reinforced concrete element was the one component model, where rotational springs are added to the ends of the elastic element to simulate the formation of plastic hinges at the extremities of the element (ref. 4). The stiffnesses of the linear elastic element stiffness and the springs was condensed using the flexibility formulation.

The determination of the characteristics of each reinforced concrete section was based on the stress strain diagrams for the concrete and the reinforcing steel. The yielding and ultimate moments for each cross section were used to determine the characteristics of the springs for each element. The spring stiffness was considered infinite whenever the element moment was below the yielding moment. When the moment was above the yielding value the spring stiffness was updated and, since there was no incremental loading or unbalanced iteration of the structure, the secant stiffness was adopted for the spring stiffness (ref. 5).

ONE COMPONENT MODEL AND MATERIAL CHARACTERISTICS

Linear Elastic Element

Spring with Secant Stiffness

One Component Reinforced Concrete Element

f_s - steel stress
f_y - yielding stress

strain

Steel Stress-Strain Diagram

f_c - concrete stress

0.002

strain

Concrete Stress-Strain Diagram

49

Procedure Implementation

The objective function was the cost of the materials: concrete and steel. The constraints included the equilibrium equalities, maximum global displacements and maximum probability of failure for each element. The equilibrium constraints were evaluated every time a design variable changed with the corresponding updating of the spring stiffnesses. The values of the maximum displacements were dictated by serviceability constraints like maximum joint rotations or story drifts. The maximum element probabilities of failure were chosen with current practices of structural design codes (ref. 6).

Flexural element actions are the most important in small and medium sized frames for the definition of section sizes and longitudinal steel. The evaluation of element reliability was based on the corresponding flexural failure function (ref. 7). The same approach was used to evaluate the system probability of failure. The basic variables considered were the compressive strength of concrete and the external loads.

The system probability of failure was evaluated at the mechanism level at the end of each optimization cycle. If the value of the system probability of failure was not satisfactory the optimization was restarted using a different limit of element probability of failure for the elements involved in the failure mechanism. The system probability of failure was obtained using the beta-unzipping method (ref. 8). In summary, the elementary mechanisms of failure were determined using Watwood's method (ref. 9) and the correspondent failure functions formed. These mechanisms were then combined linearly and the related probabilities of failure calculated, while rejecting those combinations with values outside given intervals.

SPRING SECANT STIFFNESS
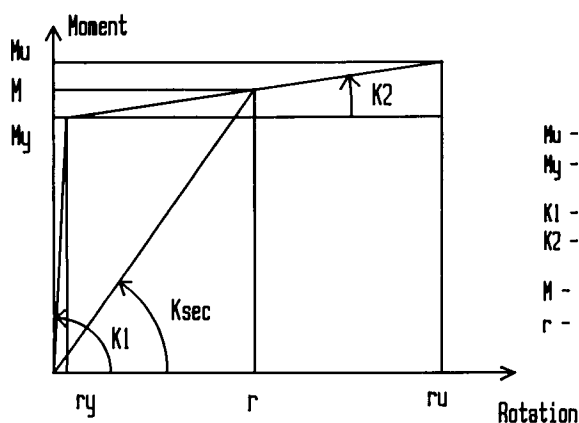
Spring Moment-Rotation Diagram

Mu – Ultimate moment   ru – Ultimate rotation
My – Yielding moment   ry – Yielding rotation

K1 – 10e30
K2 – (Mu-My)/(ru-ry)   Ksec – Spring stiffness for
                                      M > My

M – actual element moment
r – actual element chord rotation

Optimization Results

The first approach to solve the optimization problem used the Augmented Lagrangian function and the Hooke and Jeeves method as the unconstrained minimization technique. Considerable effort was put into this formulation with several options for the starting points, combinations of penalty parameters, scaling techniques and number of cycles. Three structures were tested with different levels of complexity.

In some cases the values obtained were close with those corresponding to the expected optimal values. Reliability constraints were satisfied, displacements were within the limits and equality constraints were satisfied. However, convergence was difficult to obtain and largely dependent on several different choices made at the start of the optimization cycle. At the same time the element forces were not in accordance with the assumed secant spring stiffnesses showing lack of convergence of the nonlinear iteration process.

To improve convergence of the nonlinear equilibrium of the structure an intermediate phase was created in the optimization process. The displacements were removed from the optimization cycle. This phase corresponded to the solution of the equilibrium equations every time a cycle of variable optimization in the Hooke and Jeeves was completed. The displacements were obtained from the equilibrium equations assuming the values of the secant spring stiffnesses as those at the end of the cycling optimization. The results were nevertheless the same as before and for that reason another technique was implemented.


EXAMPLES TESTED
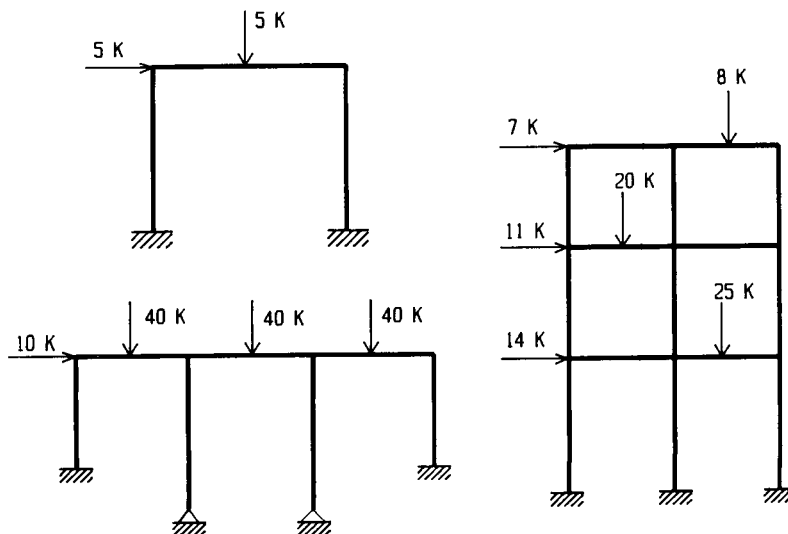
The Generalized Reduced Gradient method was chosen because of it's characteristic of solving iteratively a set of nonlinear equations. The algorithm used (ref. 10) performed very well for the elastic case with convergence in most of the cases. It proved to be almost insensitive to the initial design points. The extension to the nonlinear material behavior is however in process. A first phase of this extension consisted of assuming for the secant spring stiffness a yielding value, i.e., corresponding to the ratio of the yielding moment and the yielding rotation whenever the element moment was greater than the yielding moment. Equilibrium constraints were satisfied, element moments were in accordance with the assumed spring stiffnesses and the global displacements were in accordance with assumed spring stiffness values.

The second phase of transforming the spring stiffness from the yielding stiffness to the secant stiffness is presently being researched. The initial design for the values presented using the secant spring stiffness formulation was obtained with the elastic stiffness version having as ultimate moment the yielding moment. The secant stiffness values were limited to a minimum value corresponding to the ratio of the ultimate moment and the ultimate rotation to prevent severe oscillations of these values. The results verified the equilibrium constraints within certain tolerance, the global displacements were those corresponding to the element spring stiffnesses, reliability constraints were satisfied and there was an improvement of the cost of the structure. All elements have yielded corresponding to the expected results from a optimal configuration. However, there are discrepancies in the moments at the joints which shows a insufficient convergence of the equilibrium constraints.

RESULTS WITH YIELDING STIFFNESS AND SECANT STIFFNESS
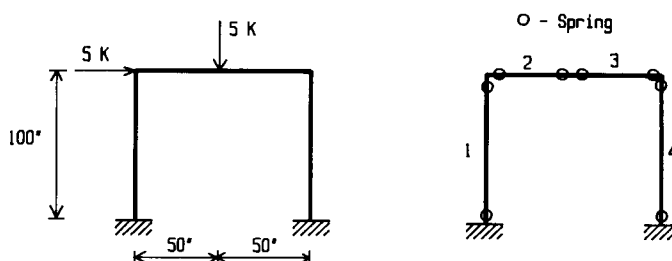
ELE MENT	INITIAL			ELASTIC			YIELDING			SECANT		
	b	h	As	b	h	As	b	h	As	b	h	As
1	5.0	10.0	1.0	2.0*	6.0*	.20	2.0*	6.0*	.21	2.0*	6.0*	.38
2	5.0	10.0	1.0	2.0*	6.0*	.23	2.0*	6.0*	.21	2.0*	6.0*	.25
3	5.0	10.0	1.0	2.0*	11.1	.73	2.0*	9.75	.64	2.0*	9.81	.64
4	5.0	10.0	1.0	2.0*	12.4	.81	2.0*	10.9	.71	2.0*	10.9	.72
Cost	18,000			6,890			6,296			6,505		

b - base (in); h - height (in); As - steel area (in2); * - lower bounds.

52

Directions Headed

The Augmented Lagrangian function together with the Hooke and Jeeves for the unconstrained minimization although insensitive to discontinuities of the constraints is not the best choice when compared with the Generalized Reduced Gradient method. More research has to be done on the robustness of the convergence of the nonlinear iteration process (ref. 11).

A possible improvement would consist of a similar enhancement to the one applied in the Augmented Lagrangian formulation with an intermediate solution of the displacements during the optimization cycle. Another possible improvement would be the use of a cycling procedure where the spring stiffness values were kept constant during the optimization and updated at the end with consequent optimization cycle until there was stabilization of the spring stiffness values.

The integrated approach proved itself adequate for the elastic stiffness if an adequate mathematical programming technique is chosen. It is logical to expect that it will probably perform well in the case of inelastic stiffness if adequately integrated with some kind of nonlinear structural analysis technique.

REFERENCES

1. Schmit, Lucien A. Jr.; and Fox, Richard L.: An Integrated Approach to Structural Synthesis and Analysis. AIAA Journal, Vol. 3, No. 6, 1960, pp. 1104-1112.

2. Haftka, Raphael T.: Simultaneous Analysis and Design. AIAA Journal, Vol. 23, No. 7, 1985, pp. 1099-1103.

3. Soeiro, Alfredo: Integrated Analysis and Optimal Design. Thesis for the Degree of Master of Engineering, University of Florida, Gainesville, 1986.

4. Charney, Finley A.: Correlation of the Analytical and Experimental Seismic Response of a 1/5th-Scale Seven-Story Reinforced Concrete Frame-Wall Structure. PhD Dissertation, University of California, Berkeley, 1986.

5. Chajes, Alexander; and Churchill, James E.: Nonlinear Frame Analysis by Finite Element Methods. ASCE Journal of Structural Engineering, Vol. 113, No. 6, 1987, pp. 1221-1235.

6. Augusti, G.; Baratta, A.; and Casciatti, F.: Probabilistic Methods in Structural Engineering. Chapman and Hall, New York, 1984.

7. Leporatti, Ezio: The Assessment of Structural Safety. Research Studies Press, Oregon, 1979.

8. Thoft-Christensen, Palle; and Morotsu, Yoshisada.: Application of Structural Systems Reliability Theory. Springer-Verlag, Berlin, 1986.

9. Watwood, Vernon: Mechanism Generation for Limit Analysis of Frames. ASCE Journal of Structural Division, Vol. 109, 1979, pp.1-15.

10. Lasdon, L. S.; Warren, A. D. Warren; Jain, A.; and Ratner, M.: Design and Testing of a Generalized Reduced Gradient Code for Nonlinear Programming. ACM Transactions on Mathematical Software, Vol. 4, No.1, 1978, pp. 34-50.

11. Soeiro, Alfredo: Integrated Optimization of Reinforced Concrete Frames with Reliability Constraints. PhD Dissertation, University of Florida, Gainesville. (To be printed in 1989.)

ERROR ANALYSIS FOR SEMI-ANALYTIC DISPLACEMENT DERIVATIVES WITH RESPECT TO SHAPE AND SIZING VARIABLES

Peter A. Fenyes and Robert V. Lust
Engineering Mechanics Department
General Motors Research Laboratories
Warren, Michigan 48090-9057

INTRODUCTION

Sensitivity analysis is fundamental to the solution of structural optimization problems. Consequently, much research has focused on the efficient computation of static displacement derivatives (Ref. 1). As originally developed, these methods relied on analytical representations for the derivatives of the structural stiffness matrix (K) with respect to the design variables (b_i). To extend these methods for use with complex finite element formulations and facilitate their implementation into structural optimization programs (eg. Ref. 2) using general finite element analysis codes (Refs. 3-4), the semi-analytic method (Refs. 5-6) was developed. In this method we approximate the matrix $\partial K / \partial b_i$ by finite difference.

Although it is well known that the accuracy of the semi-analytic method is dependent on the finite difference parameter, recent work (Ref. 7) has suggested that more fundamental inaccuracies exist in the method when used for shape optimization. Another study (Ref. 8) has argued qualitatively (for the case of a cantilevered beam) that these errors are related to non-uniform errors in the stiffness matrix derivatives.

In the following we will investigate the accuracy of the semi-analytic method. We first develop a general framework for the error analysis and then show analytically that the errors in the method are entirely accounted for by errors in $\Delta K / \Delta b_i$. Furthermore, we demonstrate that acceptable accuracy in the derivatives can be obtained through careful selection of the finite difference parameter.

Static displacement derivatives:

$$\frac{\Delta u}{\Delta b_i} = -K^{-1}\frac{\partial K}{\partial b_i}u = -K^{-1}p^s_i$$

In the semi-analytic method we approximate $\dfrac{\Delta K}{\Delta b_i} \cong \dfrac{\partial K}{\partial b_i}$ by finite differences to compute the approximation $\dfrac{\Delta u}{\Delta b_i} \cong \dfrac{\partial u}{\partial b_i}$ efficiently

This gives the semi-analytic formula $\boxed{\dfrac{\Delta u}{\Delta b_i} = -K^{-1}\dfrac{\Delta K}{\Delta b_i}u = -K^{-1}\hat{p}^s_i}$ which has been used successfully for sizing optimization.

> Barthelemy & Haftka - demonstrated large errors for shape optimization
> Pedersen, Cheng, & Rasmussen - some analysis of these errors

Figure 1

ACCURACY OF THE SEMI-ANALYTIC METHOD

To characterize the errors associated with the semi-analytic method let us examine the expression for $\Delta u/\Delta b_i$ in terms of the approximate pseudo-load vector $\tilde{p}_i^s$ (see figure 2) and consider two cases. In both cases K is separated into two parts ($\bar{K}$ and $K(b_i)$) which are independent of and dependent on the design variable b_i, respectively. In the first case we can factor $K(b_i)$ into a constant matrix K_{b_i} and a scalar function $f(b_i)$. As a result, the approximate pseudo-load vector is a simple scaling of the true pseudo-load vector p_i^s and the semi-analytic method yields displacement derivatives which are scaled with respect to the analytic derivatives. In this case the accuracy of the derivative is only dependent on the accuracy of $\Delta f/\Delta b_i$.

If, as is often the case, $K(b_i)$ can not be factored as described above then the errors in the displacement derivatives may have a significantly different form. In this case the approximate pseudo-load vector is not a simple scaling of the true pseudo-load vector. Geometrically, this means that both the shape and length of the approximate pseudo-load vector may be incorrect. Also, since $\tilde{p}_i^s$ is a function of both the error matrix E_i and the displacement field, u, the accuracy of the derivatives may depend on the number of elements in the structural model and the location, within the model, of the element(s) dependent on b_i.

Derivative given by $\dfrac{\Delta u}{\Delta b_i} = -K^{-1}\tilde{p}_i^s$ where $p_i^s = \dfrac{\Delta K}{\Delta b_i}u$

- **K factorable** in b_i : $K = \bar{K} + f(b_i)K_{b_i}$

$$\tilde{p}_i^s = \frac{\Delta f(b_i)}{\Delta b_i}K_{b_i}u = (1 + \varepsilon_i)\frac{\partial f(b_i)}{\partial b_i}K_{b_i}u = (1 + \varepsilon_i)p_i^s$$

> Thus the derivatives **scale**: $\dfrac{\Delta u}{\Delta b_i} = (1 + \varepsilon_i)\dfrac{\partial u}{\partial b_i}$

- **K not factorable** in b_i : $K = \bar{K} + K(b_i)$

$$\tilde{p}_i^s = \frac{\Delta K(b_i)}{\Delta b_i}u = \left(\frac{\partial K(b_i)}{\partial b_i} + E_i\right)u = p_i^s + E_i u$$

> Derivatives **do not scale**: $\dfrac{\Delta u}{\Delta b_i} = \dfrac{\partial u}{\partial b_i} - K^{-1}(E_i u)$

Figure 2

EXAMPLE - CANTILEVERED BEAM

To illustrate these ideas, consider a cantilevered beam modeled as an assemblage of beam type finite elements. The element level stiffness matrix for the n-th element is shown in figure 3. Clearly, K_e (and thus K) is factorable for the element height (h) and width (w) variables but is not factorable for the length variable (l). Quantitatively then (based on our previous arguments) we expect the following when using the semi-analytic method: since w appears linearly, the derivatives of the displacements with respect to w will be exact and the relative error in the derivatives of the displacements with respect to h will be uniform and depend only on the accuracy of $\Delta h^3/\Delta h$. However, the relative error in the displacement derivatives with respect to l may be non-uniform and may depend on the number of elements used to model the beam as well as on the accuracy of $\Delta K/\Delta l$. To confirm this, we will now derive analytical expressions for the relative error in these displacement derivatives.

Consider the finite element formulation for a beam element:

$$\mathbf{K}^e_n = \frac{2EI_n}{l_n^3}\begin{bmatrix} 6 & -3\,l_n & -6 & -3\,l_n \\ \vdots & 2l_n^2 & 3\,l_n & l_n^2 \\ \vdots & \cdot & 6 & 3\,l_n \\ sym & \ldots & \ldots & 2\,l_n^2 \end{bmatrix}$$

where: $I_n = \dfrac{w_n h_n^3}{12}$

Clearly, $\mathbf{K}^e_n$ may be factored for the sizing variables h and w but not for the shape variable l

Figure 3

ERROR ANALYSIS FOR THE CANTILEVERED BEAM

Consider the initially uniform cantilevered beam of length L shown in figure 4. The beam has a rectangular cross section and is subject to concentrated force (F) and moment (M) loadings at the tip. In order to investigate the accuracy of the tip displacement derivatives we can derive analytical expressions for the semi-analytic derivatives and compare them to the known true derivatives (Ref. 9). We begin with the expressions for the displacements and rotations along the length of the beam as shown below. Now let the beam be composed of N elements of length $l=L/N$ numbered from 1 to N, starting at the root. If the nodes are numbered from 0 to N, starting at the root, then the n-th node is located an $x=nl$. Substituting for x in the equations for u and θ yields a set of discretized equations for u and θ. To complete the derivation we need expressions for the entries of K^{-1} associated with the tip displacement d.o.f. and for the derivatives of the stiffness matrix with respect to the design variables b_n. The stiffness matrix derivatives are easily derived from the expression for the element level stiffness matrix shown previously. The necessary entries of K^{-1} can be obtained by differentiating the displacement vector with respect to the applied force (F). Substitution of these expressions into the equation for the tip displacement derivative will yield the desired analytical expression for the semi-analytic derivative.

We can determine analytical expressions for the errors introduced by finite differencing in the S-A method by using the exact beam element formulation.
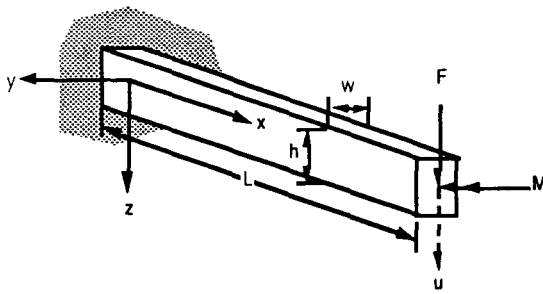
$$u(x) = \frac{(FL-M)x^2}{2EI} - \frac{Fx^3}{6EI}$$

$$\theta(x) = \frac{Fx^2}{2EI} + \frac{(M-FL)x}{EI}$$

Discretizing for a beam of N elements we can compute:

$$\frac{\Delta u^t}{\Delta b_n} = -\{K^{-1}\}^T \frac{\Delta K}{\Delta b_n} u \quad \text{where} \quad \{K^{-1}\}^T = \frac{\partial u}{\partial F}$$

Figure 4

59

ERROR ANALYSIS FOR THE CANTILEVERED BEAM

In figure 5 the expressions for the semi-analytic tip displacement derivatives with respect to the element heights and lengths (in terms of the exact derivatives) are shown. The expressions have been simplified to the case where $F=0$. For h, the stiffness matrix is factorable and, as was predicted, the relative error (ε) depends only on the finite difference parameter (c) and is the same for all elements making up the beam. For the element lengths, K is not factorable and the relative error is non-uniform. In this case the relative error depends not only on c, but also on the element number (n) and the number of elements (N) used to model the beam. Increasing either n or N will cause the relative error to become larger, while decreasing the value of c will give better accuracy. In Refs. 7 and 8 the tip displacement derivatives with respect to L ($\Delta u^t/\Delta L$) are investigated. This quantity is based on perturbations of all elements in the beam such that the quantity ΔL is distributed evenly among all elements. In this case the relative error in $\Delta u^t/\Delta L$ is equivalent to the average error (ε_{avg}) in $\Delta u^t/\Delta l_n$. For small values of c, ε_{avg} is approximately proportional to cN^2. Note that, as would be expected, in all cases the relative error approaches zero as c approaches zero.

- **Factorable** sizing variable h : $K= \bar{K} + f(h^3)K_h$

> Relative error is a function of c only: $\dfrac{\Delta u^t}{\Delta h} = (1+ \dfrac{c^2 + 3c}{3})\dfrac{\partial u^t}{\partial h}$

- **Non-factorable** shape variable l : $K = \bar{K} + K(l_n)$

> Relative error is a function of c, n, and N :
>
> $$\frac{\Delta u^t}{\Delta l_n} = \frac{\partial u^t}{\partial l_n}\left[\frac{2N -c^2(2n-2N-1) +c(12n^3 -24\ n^2 N -18\ n^2 + 24nN+ 8n -2N + 1)}{2N(c+1)^3}\right]$$
>
> $$= \frac{\partial u^t}{\partial l_n}(1+ (\varepsilon(c,n,N)))$$

> Average error is a function of c, and N :
>
> $$\varepsilon_{avg} = \frac{1}{N}\sum_{n=1}^{N}\varepsilon(c,n,N) = \frac{1-c(\frac{5}{2}N^2 -2 -1/N)}{(c+1)^3} -1$$

Figure 5

COMPUTATIONAL RESULTS: SHAPE VARIABLES

To demonstrate the analytical results presented previously the cantilevered beam was modeled with beam elements and the tip displacement derivatives with respect to the element lengths were calculated numerically via the semi-analytic method. In the figure below these derivatives (for $c=.01$) are plotted (normalized by the true derivative) versus the element number for four different beam discretizations (5,10,15 and 20 elements). The numerically generated data points are represented by the symbols shown on the plot. The analytic results appear as the underlying curves. Note that the computed values are in complete agreement with the analytic values. As predicted, the relative error depends on both n and N. For this problem, the error increases with N and increases as we move along the beam from the root to the tip.

In figure 6 we also show the **average** error of the tip displacement derivatives, with respect to the element length, as a function of the number of elements in the beam. In this case the computed and predicted values are plotted for various values of c. In addition, the equivalent numerical data from Ref. 7 (represented by the square symbols) is also shown. Note, again, the excellent agreement between the computed and predicted errors. Clearly, the error decreases rapidly as c is decreased. For $c=.00001$ the average error is less than 1.0%. for $N=20$.
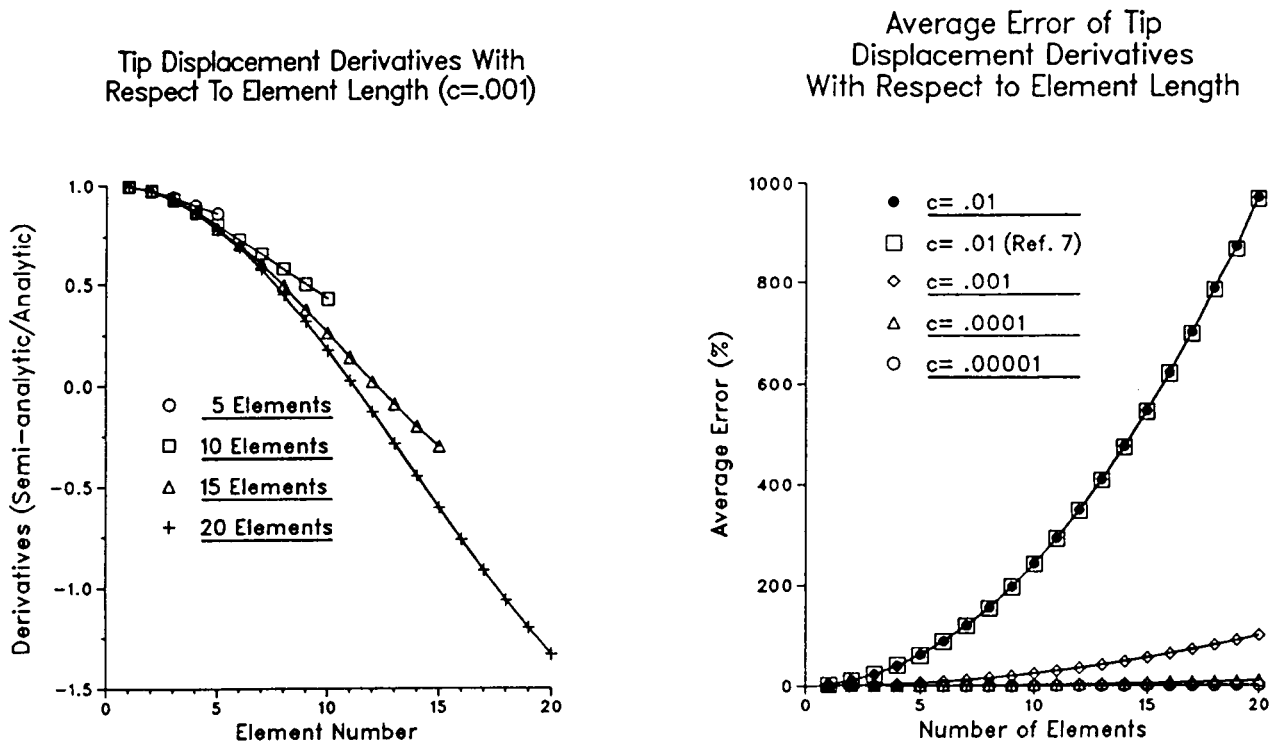

Figure 6

ERROR ANALYSIS FOR NON-PLANAR BEAM

We have seen that for the cantilevered beam problem uniform errors occur for the tip displacement derivatives with respect to sizing design variables and nonuniform errors occur for shape variables. However, our general error analysis predicts that the nature of the error depends on the factorability of K and not necessarily on the classification of the design variable. We will now show that nonuniform derivative errors can (and usually do) occur for sizing design variables.

Consider the case of a rectangular cantilevered beam where the principal axes of the beam elements are oriented at some angle to the global coordinate system. In this case the stiffness matrix is not generally factorable for w and h since both variables contribute to the stiffnesses in the global coordinate system. As a result nonuniform error in the global displacement derivatives may occur. To investigate this analytically, consider the equivalent system shown in figure 7 where we want to calculate the derivative of the displacement at some angle θ to the beam's principal axes ($\Delta d^t / \Delta b_n$). Using our previous analysis for displacement derivatives in the principal coordinate system we can develop the expression shown below for the relative error (ε_n) associated with $\Delta d^t / \Delta b_n$ (Ref.9). As shown, ε_n is a function of the relative errors associated with the principal displacement derivatives Generally, they combine such that ε_n will differ for each element. Under certain conditions, however, uniform errors will occur. Clearly, this will be the case when θ is some multiple of $\pi/2$. Uniform error will also occur when the loading in y and z directions are related by a scaling factor since the resulting displacements and displacement derivatives will also be simply scaled.
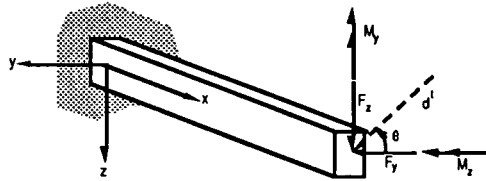
$$d^t = u^t \cos\theta + v^t \sin\theta$$

For sizing variables:

$$\frac{\Delta u^t}{\Delta b_n} = (1+ \varepsilon^u)\frac{\partial u^t}{\partial b_n}$$

$$\frac{\Delta v^t}{\Delta b_n} = (1+ \varepsilon^v)\frac{\partial v^t}{\partial b_n}$$

The relative error of the displacement derivative is given by :

$$\varepsilon_n = \frac{\dfrac{\Delta d^t}{\Delta b_n} - \dfrac{\partial d^t}{\partial b_n}}{\dfrac{\partial d^t}{\partial b_n}} = \frac{\varepsilon^u \dfrac{\partial u^t}{\partial b_n}\cos\theta + \varepsilon^v \dfrac{\partial v^t}{\partial b_n}\sin\theta}{\dfrac{\partial u^t}{\partial b_n}\cos\theta + \dfrac{\partial v^t}{\partial b_n}\sin\theta}$$

- **Uniform error** when $\theta = i\pi/2$ or $P_z = \gamma P_y$

- **Non-uniform error** otherwise

Figure 7

62

NONUNIFORM ERRORS - SIZING VARIABLES

To numerically illustrate that nonuniform errors can occur for displacement derivatives with respect to sizing design variables we calculated the derivative of the tip displacement for a cantilevered beam with respect to the element heights using the semi-analytic method. The beam was rotated so that its principal axes were oriented at 45 degrees relative to the global coordinate system. A tip force and moment were applied parallel to the global axes. In figure 8 the derivatives are plotted (normalized by the analytic derivatives) as a function of the element number for $c=0.01$ and various beam discretizations (5,10,15 and 20 elements). As expected, the derivatives depend on the element number and the number of element used to model the beam. In this case the relative error decreases with increasing N and decreases as we move along the beam from the root to the tip.

In figure 8 we also show the normalized tip displacement derivatives plotted versus the element number for $N=20$ and various values of c. Note that the relative error decreases rapidly as c is decreased. Also, the magnitudes of the errors are significantly less, for a given value of c, than we found for the derivatives with respect to the element lengths. For $N=20$, acceptable accuracy is obtained for values of c as large as 0.01.
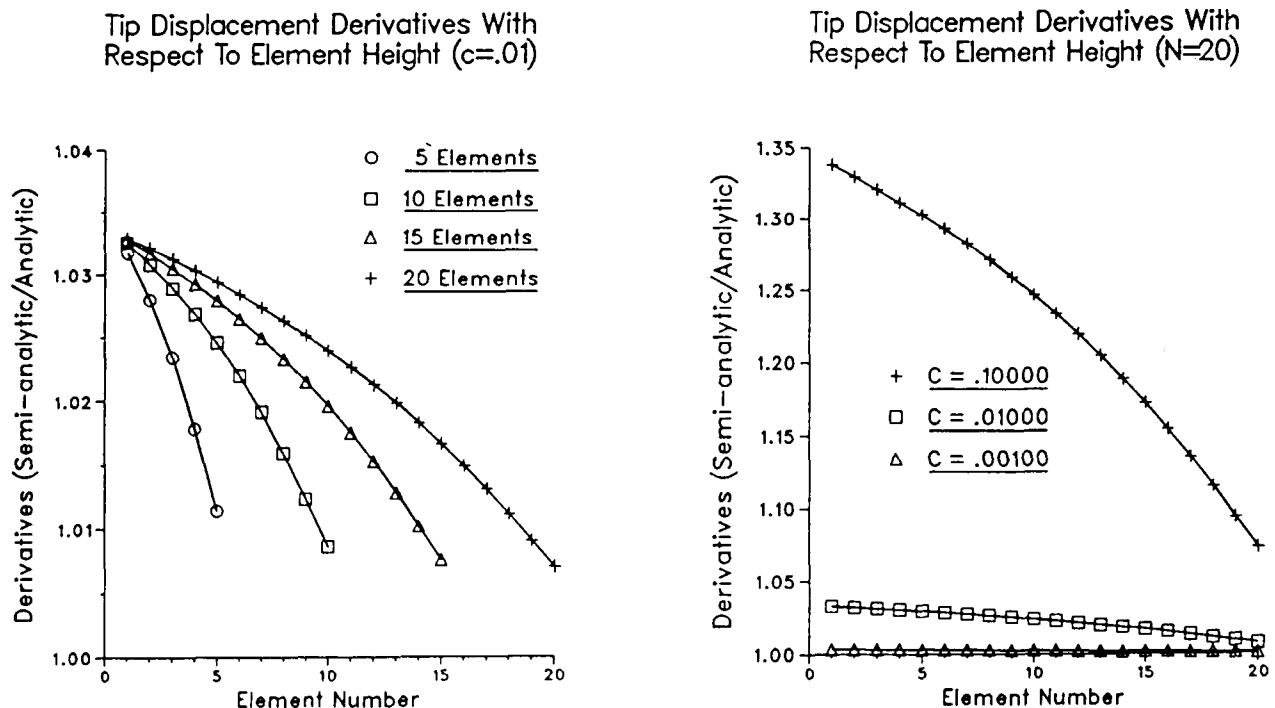

Figure 8

ERROR ANALYSIS - AUTOMOTIVE FRAME

To study the accuracy of the semi-analytic method for more practical problems, consider the half model of an idealized automobile frame structure shown in figure 9. The structural model consists of 33 three-dimensional beam-type finite elements each having a rectangular cross section. The structure is simply supported at the front suspension attachment points (A) and loaded in the vertical direction at the rear suspension attachment points (B). Boundary conditions are applied to the center line grid points to enforce an anti-symmetric structural response. The net effect of the loading and boundary conditions is to cause torsion of the structure about the centerline. In this case we calculated the semi-analytic derivatives of the vertical displacement at point C with respect to the thickness, width, height and length of each element in the structure and compared them against the analytic derivatives. In all cases the accuracy of the derivatives varies from element to element. The results of the comparison are summarized in the plot below. For each type of design variable (length, height, width and thickness) the minimum, maximum and average errors in semi-analytic derivatives are plotted as a function of the finite difference parameter (c). Note that each type of design variable exhibits a different level of accuracy, for a given value of c, with the length variable being the worst and thickness being the best. This can be attributed to the varying degrees of nonlinearity of the stiffness matrix with respect to these variables. For a thin walled box beam the section properties are nearly linear functions of t and therefore the accuracy of the displacement derivatives with respect to t is much better than that for b, h and l. In general, the careful selection of design variables or other intermediate variables (e.g., beam section properties) for the derivative calculations will yield more accurate derivatives for any given value of c.
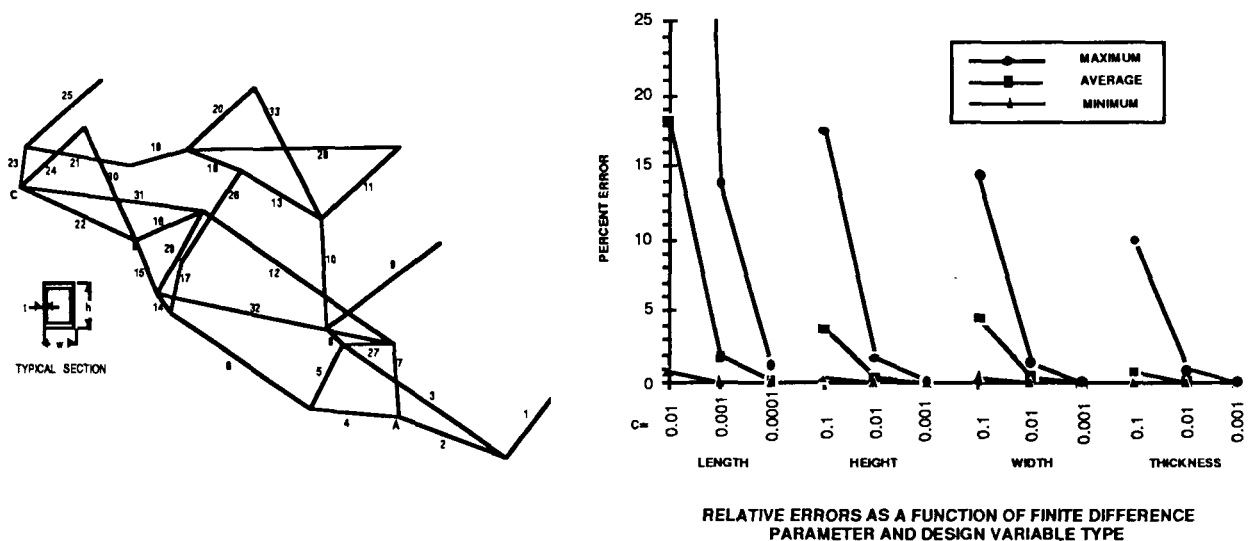

RELATIVE ERRORS AS A FUNCTION OF FINITE DIFFERENCE
PARAMETER AND DESIGN VARIABLE TYPE

Figure 9

SUMMARY

The inaccuracy of the semi-analytic method for computing static displacement derivatives for both shape and sizing design variables has been shown to be the result of errors in the pseudo load vectors. Two types of errors were identified. In the first case the errors in the finite difference approximation to the stiffness matrix derivatives resulted in a scaling of the pseudo load vector which, in turn, causes the derivatives to be uniformly scaled relative to their true values. In this case the magnitude of the error depends only on the finite difference parameter, c. In the second case, errors in the finite difference operation lead to a distortion of the pseudo load vectors and nonuniform errors in the displacement derivatives. These errors may be dependent on the location (within the structure) of the element(s) associated with the design variable and the discretization of the structure, as well as c.

The results of the error analysis were demonstrated numerically for a cantilevered beam and an idealized automobile frame structure. It was observed that for a given value of c that the errors in the derivatives for shape design variables were significantly larger than those for sizing variables. However, in both cases the relative errors could be adequately controlled through the proper choice of the finite difference parameter. It should be noted that relatively small values for c may be required to compute sufficiently accurate derivatives. This suggests that it may be necessary to compute the finite difference approximations to the stiffness matrix derivatives in double precision to avoid roundoff errors. Also, by carefully choosing intermediate variables which appear linearly (or nearly so) in the stiffness matrix, greater accuracy in the the finite difference approximation can be obtained.

- Errors reported for the semi-analytic method have been shown to be due to errors in the finite difference approximation of the stiffness matrix derivatives

  - We can adequately control errors by careful choice of the finite difference parameter

- Errors may occur for both shape and sizing variables

  - For a given value of the finite difference parameter, errors in the derivatives of the shape variables were larger than the sizing variables

---

Figure 10

REFERENCES

1. Adelman, H. M. and Haftka, R. T., "Sensitivity Analysis of Discrete Structural Systems," <u>AIAA Journal</u>, Vol. 24, No. 5, May 1986, pp. 823-832.

2. Bennett, J. A. and Nelson, M. F., "An Optimization Capability for Automotive Structures," <u>SAE Transactions</u>, Vol. 88, 1979, pp. 3236-3243.

3. Botkin, M. E., Lust, R. V., Song, J. O., Yang, R. J., Katnik, R. B., "Structural Sizing Optimization Using an External Finite Element Program," <u>Proceedings of the 28th AIAA/ASME/ASCE/AHS Structures, Structural Dynamics and Materials Conference - Part 2A</u>, Monterey, California, April 6-8, 1987, pp. 513-521.

4. Wallerstein, D. V., "Application Note on Design Sensitivity Analysis," MacNeal-Schwendler Corporation, March 11, 1983.

5. Botkin, M. E., "Shape Optimization of Plate and Shell Structures," <u>AIAA Journal</u>, Vol. 20, No. 2, Feb. 1982, pp.268-273.

6. Camarda, C. J. and Adelman, H. M., "Static and Dynamic Structural-Sensitivity Derivative Calculations in the Finite-Element-Based Engineering Analysis Language (EAL) System," NASA TM-85743, March 1984.

7. Barthelemy, B. and Haftka, R. T., "Accuracy of the Semi-Analytical Method for Shape Sensitivity Calculations," <u>Proceedings of the 29th AIAA/ASME/ASCE/AHS Structures, Structural Dynamics, and Materials Conference, Part 1</u>, Williamsburg, VA, April 18-20, 1988, pp. 572-588.

8. Pederson, P., Cheng, G., and Rasmussen, J., "On Accuracy Problems for Semi- Analytical Sensitivity Analyses," Danish Center for Applied Mathematics and Mechanics Report No. 367, December, 1987.

9. Fenyes, P. A. and Lust, R. V., "Error Analysis for Semi-analytic Displacement Derivatives With Respect to Shape and Sizing Variables," General Motors Research Report No. 6561, February 10, 1989.

ACOUSTIC EMISSION FROM A GROWING CRACK

Laurence J. Jacobs
Engineering Science and Mechanics Program
School of Civil Engineering
Georgia Institute of Technology
Atlanta, Georgia   30332

ABSTRACT

An analytical method is being developed to determine the signature of an acoustic emission waveform from a growing crack and the results of this analysis are compared to experimentally obtained values. Within the assumptions of linear elastic fracture mechanics, a two dimensional model is developed to examine a semi-infinite crack that, after propagating with a constant velocity, suddenly stops. The analytical model employs an integral equation method for the analysis of problems of dynamic fracture mechanics. The experimental procedure uses an interferometric apparatus that makes very localized absolute measurements with very high fidelity and without acoustically loading the specimen.

INTRODUCTION

Acoustic emission testing is a method of nondestructive evaluation that detects stress wave emissions from fracture and deformation processes within a loaded body. This testing differs from other methods of nondestructive evaluation in that the signal being detected is released from within the specimen rather than being created by the nondestructive testing method. The technique offers a distinct advantage over more conventional nondestructive testing techniques because it allows for the real time monitoring of in-service structures. Some of the potential source mechanisms of acoustic emission include: crack propagation and arrest, fretting among fracture surfaces, dislocation movement, microcracking, twinning and phase transformations. In addition to these failure related mechanisms, other phenomena such as fastener fretting, structural vibration and electromagnetic noise can create spurious signals which are detected by the acoustic emission instrumentation. Of fundamental importance for the advancement of the current state of acoustic emission technology is the isolation and identification of the signal from a growing crack. The technology for detecting and locating internal sources of acoustic emission is well established. However, acoustic emission signals contain a vast amount of additional information about the source of the emission and the condition of the material being examined. The signal is not only influenced by its source but also by the specimen geometry (which effects the stress wave propagation from the source to the sensor) and the characteristics of the sensor. A thorough understanding of each of these factors is necessary in order to accurately interpret the acoustic emission signature. The proposed solution procedure will attempt to apply methods from dynamic fracture mechanics and wave propagation to the quantitative characterization of acoustic emission signals.

This work complements previous studies by providing a development of the analytical form of an acoustic emission waveform caused by a crack growth event. An advantage of the proposed analysis is that the source for the acoustic emission signature is an actual crack propagation event and not a simple point source model. The propagation of the crack greatly influences the stress field in the vicinity of the crack tip, causing stress wave fronts to radiate into the body and on the crack surface. Acoustic emission testing detects these stress waves at the body's surface and relates the signal back to the corresponding crack propagation event. The proposed method uses an integral equation technique for the analysis of problems of dynamic fracture mechanics developed by Jacobs and Bieniek [1]. The problems of dynamic crack propagation have been the subject of numerous investigations in the past several years. A majority of the work

has been summarized in review articles by Achenbach [2, 3], Freund [4, 5], Rose [6] and in the book by Kanninen and Popelar [7]. The preceding works have primarily been concerned with the determination of the dynamic stress field in the vicinity of the moving crack tip. They did not examine the effect of the propagation and arrest of the crack tips throughout the entire body. Freund [8] determined the pressure discontinuity radiated out from a crack tip when the crack, which is initially at rest, begins to grow. Rose [9] calculated explicit formulae for the stress discontinuities radiated by a suddenly starting two dimensional crack under tension for application to acoustic emission testing. Achenbach and Harris [10] examined the acoustic emission signals from a semi-infinite crack of arbitrary shape using the elastodynamic ray theory. Harris and Pott [11] investigated the surface motions excited by fracture processes at the edge of a buried crack.

Previous investigators worked to identify the acoustic emission signal from a crack propagation and arrest source. Summaries of this work appears in Eitzen and Wadley [12], Pao [13] and in a book by the American Society for Nondestructive Testing [14]. Hutton, Friesel, Graham and Elsley [15] successfully characterized acoustic emission signals in laboratory investigations using statistical pattern recognition algorithms which characterize signals empirically on the basis of features observed in a large number of events. These methods are strictly empirical in nature and provide little insight into the fracture process. Other investigators concentrated on the geometrical effects of the acoustic emission signal. Pao, Gajewski and Ceranoglu [16] and Ceranoglu and Pao [17, 18, 19] examined the propagation of an acoustic emission signal in an elastic plate. These solutions are not empirical, but are based on the generation and propagation of elastic waves in a wave guide. The solutions, which examine point sources inside an infinite elastic plate, use a generalized ray theory and integral transform techniques. They provide numerical results for the surface displacements for a variety of dynamic nuclei of strains, including concentrated forces and couples. Individual or combinations of these sources are used to model the dynamic processes of material defects. Kim and Sachse [20, 21, 22, 23] investigated both the analytical and experimental signature of an acoustic emission waveform.

ANALYTICAL METHOD

The integral equation in the present application is in two variables, a spatial coordinate (x) and time (t). Within the assumptions of linear elastic fracture mechanics, the dynamic stresses caused by a prescribed crack growth event in an infinite two dimensional body are calculated. These results can be used to calculate displacement as a function of time at any point within the body. The first step of this analysis, summarized in [24, 25], uses an influence function to formulate an integral equation that expresses the boundary conditions in the plane of the crack. The steps for the calculation of the dynamic stresses are as follows:

(a) Determination of the influence (or Green's) function of the problem, which is the dynamic displacement of an elastic half-space subjected to a unit concentrated impulse acting at the point of, and normal to, its edge.

(b) Formulation of the integral equation of the problem. This integral equation, with the influence function as the kernel and the normal stress in the plane of the crack as the unknown function, expresses the boundary conditions in the plane of the crack - a stress free crack surface and continuity of displacements outside of the crack.

(c) Solution of the integral equation.

The solution presented is for a semi-infinite crack that is symmetrically loaded (Mode I). First, solve for the influence function, $U_y(x-x',t-t')$, in closed form using integral transform methods. This is accomplished by taking a one-sided Laplace transform in time t and a two-sided Laplace transform in x. In the transform space, the two uncoupled partial differential equations are replaced by two uncoupled ordinary differential equations. The determination of the inverse transformations of the required surface displacement component is accomplished using the Cagniard-de Hoop method.

To formulate the integral equation, assume a crack exists at time t=0 with its tip located at x=a(0) and y=0. For time t>0, the crack moves from x=a(0) to x=a(t). The two relevant boundary conditions are that the newly formed crack faces are stress free and that the vertical displacement in front of the moving crack tip is zero. Both of these boundary conditions are met by:

(a) Removing the existing known static stress, σ_{yy}=P(x), and assuming that instead a new unknown time dependent stress, σ_{yy}=F(x,t), develops.

(b) Requiring that the new stress distribution be such that there is vertical displacement continuity in front of the moving crack tip.

The continuity boundary condition can be expressed in terms of the influence function, $U_y(x-x',t-t')$, as:

$$-\int_0^t \int_{-\infty}^{\infty} P_s(x')U_y(x-x',t-t')dx'dt' + \int_0^t \int_{-\infty}^{\infty} F(x',t')U_y(x-x',t-t')dx'dt' = 0 \qquad (1)$$

The above is a Volterra integral equation of the first kind in the variables x and t. To provide a simple solution of this integral equation, assume some spatial form of the unknown stress distribution, F(x',t'). Assume, further, that the spatial distribution of F(x',t') contains a square root singularity at its tip location a(t'), which is the same spatial form of stresses as a static crack with its tip located at a(t'). However, F(x',t') must contain an unknown time function, K(t'). Thus, the unknown stress in front of the moving crack tip is assumed to have the spatial form of its corresponding static crack multiplied by some unknown time function. It should be noted that due to the presence of step functions in the influence function, the infinity limits in the x' integration of the integral equation can be replaced by the distance that the fastest wave will travel in the elapsed time, t-t'.

The direct quadrature method [26, 27] is used for the solution of the integral equation. There are, however, two refinements which are necessary in the numerical solution of the integral equation. The first refinement is a "subdivision" of the time step, delta t, in the evaluation of the numerical

70

integrations, while the second is a mid-point product integration scheme [28] which is employed to handle the singularity of the kernel at $t'=t$. For the steady state case of a crack propagating with a constant velocity, the calculated value of K(t) is a constant that is only a function of the crack tip velocity. As the crack tip speed increases, the corresponding constant value of K(t) will decrease. The results of the case for a crack that suddenly stops after propagating is that the calculated value of K(t) discontinuously jumps to the value of the corresponding static stress; there is no transition zone and the stress never increases above the value for an equivalent static crack.

The displacement at any point within the infinite body is determined using the previously calculated dynamic stress, F(x,t) and two new influence functions $U_{xy}(x-x',y,t-t')$ and $U_{yy}(x-x',y,t-t')$. These influence functions represent the horizontal displacement u_x and the vertical displacement u_y, respectively, at point (x,y) within an elastic half-space that is subjected to a vertical unit impulse surface loading at x'. The solution for these new influence functions is accomplished using integral transform techniques and the inversion is again performed using the Cagniard-de Hoop method. Convolution integrals are developed for the vertical and horizontal displacements for any point, (x,y), within the body by determining the displacements due to the application of the previously calculated dynamic stress distribution and the removal of the initial static stress distribution. The displacements are given by:

$$u_x(x,y,t) = -\int_0^t \int_{-\infty}^{\infty} P_s(x')U_{xy}(x-x',y,t-t')dx'dt' + \int_0^t \int_{-\infty}^{\infty} F(x',t')U_{xy}(x-x',y,t-t')dx'dt' \quad (2)$$

$$u_y(x,y,t) = -\int_0^t \int_{-\infty}^{\infty} P_s(x')U_{yy}(x-x',y,t-t')dx'dt' + \int_0^t \int_{-\infty}^{\infty} F(x',t')U_{yy}(x-x',y,t-t')dx'dt' \quad (3)$$

These integrals can be evaluated numerically. Difficulties arise in the x' integration due to both the integrands' complexity and the presence of singularities. There are singularities of different strengths and discontinuities associated with the moving crack tip, the original crack tip and the various wave fronts. Each of these singularities must be investigated separately to properly evaluate the integrals. To avoid numerical problems, the final integration technique will involve separating the x' integration interval into singular and non-singular regions. To evaluate the integral in the area of the singularity, a hybrid method is proposed. Following Davis and Rabinowitz in [71], the singularity is dealt with by breaking up the original integral in the singular region into two new integrals. One of the new integrals contains the singularity, but it can be evaluated analytically; the second integral, which is evaluated numerically, is non-singular since its integrand will approach zero as the potential singular point is approached.

EXPERIMENTAL RESULTS

The second step is to compare the results of the analytical model with experimentally obtained waveforms. It should be noted that the analytical procedure being developed is for the time prior to the arrival of stress waves

reflected from the test specimen's boundary so it is invalid for the time period after the fastest reflected waves interfere with the unadulterated signal from the crack propagation event. The experimental test procedure examines an existing crack that is forced to propagate a short distance and be arrested. The specimen used is a screw loaded, wedge opening load sample, where the crack unloads as it extends and the propagation is arrested before complete failure occurs. The specimens are made of a brittle material with a low fracture toughness, poly methyl methacrylate. Its optical transparency permit the size, geometry and location of the cracks to be readily determined. Cracks in these specimens are initiated by driving a sharp blade into the notch of the specimen; further propagation is produced by tightening the screw.

A high sensitivity heterodyne interferometer is used to detect acoustic emission events. This optical device permits the high fidelity localized measurement of velocities from acoustic emission events arriving at various points on the sample surface. Since this type of measurement does not acoustically load the sample, the event being observed is undisturbed by the measurement process. The most commonly used acoustic emission sensor is the piezoelectric transducer. Since it must be used in direct contact with the specimen, the transducer will disturb the process being measured and the signal response will be averaged over this area of contact. Additional limitations of these sensors is that it is difficult to manufacture a truly broad band transducer, they are extremely difficult to calibrate accurately and there are many questions as to exactly what the transducer is measuring.

The specimen face opposite the crack is polished and placed in the interferometer and becomes one mirror surface. The beam striking the face is approximately 1.5 mm in diameter and samples the average displacement taking place over this region, which is much smaller than the wavelength of the acoustic events being observed. The operation of the heterodyne interferometer is described in [30]. Briefly, single frequency laser light is split into two components using an acousto-optic modulator. These two components, which are separated in frequency by 40 MHz, are sent along two arms of an interferometer one of which contains the sample being monitored. The beams are recombined on the surface of a photodetector where they beat together at a frequency of 40 MHz. Phase shifts in the light reflected from the sample surface result in equivalent phase shifts in the 40 MHz beat signal received at the photodetector. This carrier signal can then be demodulated to determine the time dependent displacement occurring at the sample surface. The detection system has a band width of 10 MHz which is further limited to the spectral region 0 to 2 MHz in order to reduce the noise in the signal. All signals are acquired on a digital oscilloscope and stored for later processing. The crack velocity is measured with conventional crack propagation gages. This also aids in determining the time difference between the crack growth event and the arrival of its signal at the measurement point. This is accomplished by pretriggering the measurement system on the start of the crack propagation event and not the arrival of the first wavefront.


DISCUSSION

A characteristic crack emission is shown in figure 1. Care must be taken to calculate the effect of wave reflections and mode conversions that occur at the specimen's boundaries. The experimentally obtained waveforms will be

interpreted using the results of the analytical model being developed in the first task. Since the dynamic stress calculations indicate sharp stress discontinuities associated with the starting and stopping phases, it is anticipated that there will be corresponding displacement variations that will become evident in the experimental modeling. Anomalies in the fracture behavior of the specimen included out of plane growth and some crack tunneling. The out of plane growth could be caused by twisting due to the bearing stress between the bolt and the lower crack surface. Further development of the analytical model is necessary before the experimentally obtained waveforms can be interpreted.

ACKNOWLEDGEMENT

Figure 1: Acoustic Emission Signal from a Growing Crack
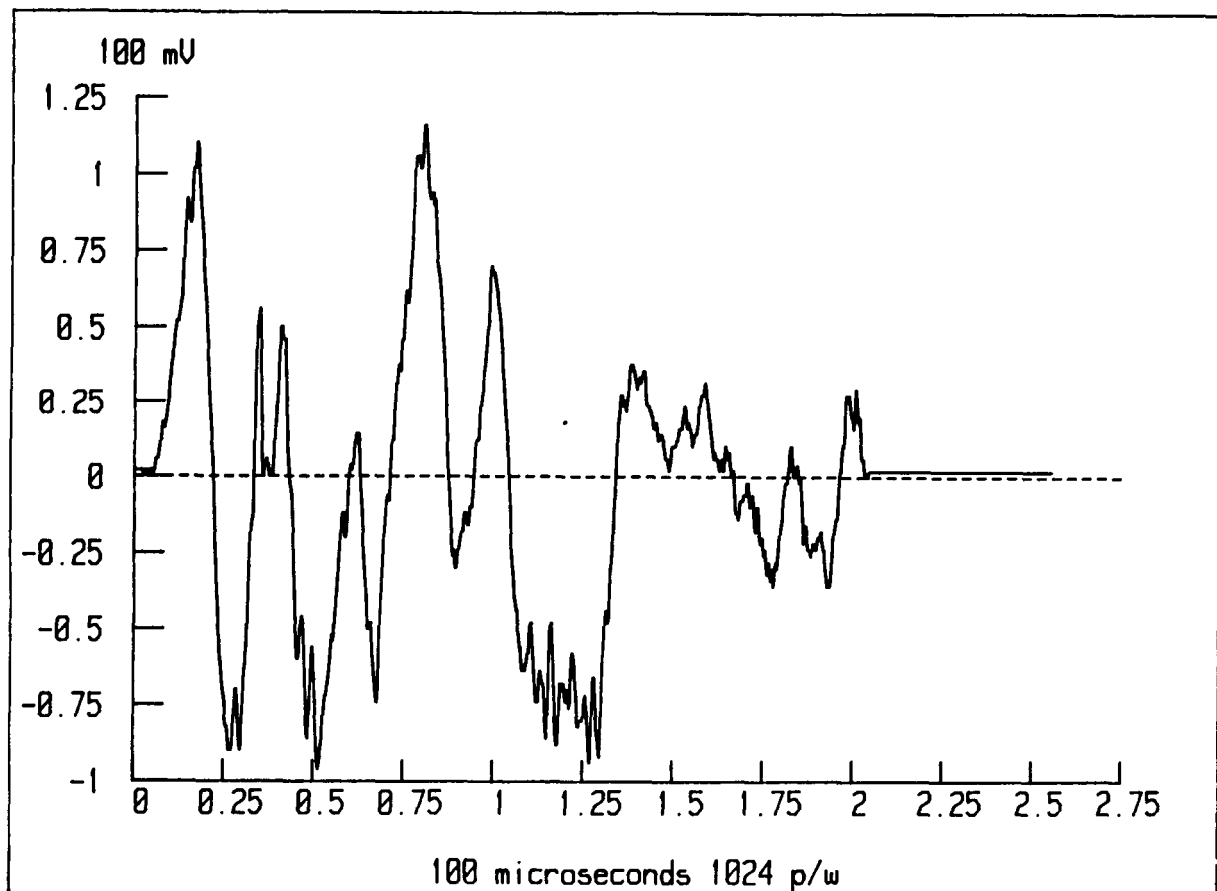
REFERENCES

1.   L.J. Jacobs and M.P. Bieniek, "An Integral Equation Method for Dynamic Crack Growth Problems," submitted to International Journal of Fracture, 1988.

2.   J.D. Achenbach, " Dynamic Effects in Brittle Fracture," in Mechanics Today, S. Nemat-Nasser, ed., Pergamon Press, Vol. 1, 1974, pp. 1-54.

3.   J. D. Achenbach, "Wave Propagation, Elastodynamic Stress Singularities, and Fracture," in Proceedings of the 14th IUTAM Congress, W.T. Koiter, ed., North-Holland Publishing, 1976, pp. 71-87.

4.   L.B. Freund, "Dynamic Crack Propagation," in The Mechanics of Fracture, ASME AMD-19, F. Erdogan, ed., 1976, pp. 105-134.

5.   L.B. Freund, "The Mechanics of Dynamic Crack Growth in Solids," in Fundamentals of Deformation and Fracture: Eshelby Memorial Symposium, B.A. Bilby, K.J. Miller and J.R. Willis, eds., Cambridge University Press, 1985, pp. 163-185.

6.   L.R.F. Rose, "Recent Theoretical and Experimental Results on Fast Brittle Fracture," International Journal of Fracture, Vol. 12, 1976, pp. 799-813.

7.   M.F. Kanninen and C.H. Popelar, Advanced Fracture Mechanics, Oxford University Press, 1985.

8.   L.B. Freund, "The Initial Wave Front Emitted by a Suddenly Extending Crack in an Elastic Solid," Journal of Applied Mechanics, Vol. 39, 1972, pp. 601-602.

9.   L.R.F. Rose, "The Stress-Wave Radiation from Growing Cracks," International Journal of Fracture, Vol. 17, 1981, pp. 45-60.

10.   J.D. Achenbach and J.G. Harris, "Acoustic Emission from a Brief Crack Propagation Event," Journal of Applied Mechanics, Vol. 46, 1979, pp. 107-112.

11.   J.G. Harris and J. Pott, "Surface Motion Excited by Acoustic Emission from a Buried Crack," Journal of Applied Mechanics, Vol. 51, 1984, pp. 77-83.

12.   D.G. Eitzen and H.N.G. Wadley, "Acoustic Emission: Establishing the Fundamentals," Journal of Research of the National Bureau of Standards, Vol. 89, 1984, pp. 75-100.

13.   Y.H. Pao, "Theory of Acoustic Emission," in Elastic Waves and Nondestructive Testing of Materials, ASME AMD-Vol. 29, 1978, pp. 107-128.

14.   R.K. Miller, Nondestructive Testing Handbook Volume 5, American Society for Nondestructive Testing, 1987.

15.   P.H. Hutton, M.A. Friesel, L.J. Graham and R.K. Elsley, Develop in-Flight Acoustic Emission Monitoring of Aircraft to Detect Fatigue Crack Growth, Final Report to the Naval Air Development Center, 1986.

74

16. Y.H. Pao, R.R. Gajewski and A.N. Ceranoglu, "Acoustic Emission and Transient Waves in an Elastic Plate," _The Journal of the Acoustical Society of America_, Vol. 65, 1979, pp. 96-105.

17. A.N. Ceranoglu and Y.H. Pao, "Propagation of Elastic Pulses and Acoustic Emission in a Plate, Part 1: Theory," _Journal of Applied Mechanics_, Vol. 48, 1981, pp. 125-132.

18. A.N. Ceranoglu and Y.H. Pao, "Propagation of Elastic Pulses and Acoustic Emission in a Plate, Part 2: Epicentral Responses," _Journal of Applied Mechanics_, Vol. 48, 1981, pp. 133-138.

19. A.N. Ceranoglu and Y.H. Pao, "Propagation of Elastic Pulses and Acoustic Emission in a Plate, Part 3: General Responses," _Journal of Applied Mechanics_, Vol. 48, 1981, pp. 139-147.

20. K.Y. Kim and W. Sachse, "Characteristics of Acoustic Emission Signals of Hertzian and Unloading Cracks in Glass," _Journal of Applied Physics_, Vol. 55, 1984, pp. 2847-2856.

21. K.Y. Kim and W. Sachse, "Acoustic Emission from Penny-Shaped Cracks in Glass. I. Radiation Pattern and Crack Orientation," _Journal of Applied Physics_, Vol. 59, 1986, pp. 2704-2710.

22. K.Y. Kim and W. Sachse, "Acoustic Emission from Penny-Shaped Cracks in Glass.II. Moment Tensor and Source-Time Function," _Journal of Applied Physics_, Vol. 59, 1986, pp. 2711-2715.

23. K.Y. Kim and W. Sachse, "Characteristics of an Acoustic Emission Source from a Thermal Crack in Glass," _International Journal of Fracture_, Vol. 31, 1986, pp. 211-231.

24. L.J. Jacobs, "Dynamic Mode I Crack Propagation," Ph.D. Dissertation, Department of Civil Engineering and Engineering Mechanics, Columbia University, New York, NY, 1987.

25. L.J. Jacobs, Xiaogong Lee and M.P. Bieniek, "Two Problems of Dynamic Fracture Mechanics," 29th Structures, Structural Dynamics and Materials Conference, Williamsburg, Virginia, April 18-20, 1988.

26. C.T.H. Baker, _The Numerical Treatment of Integral Equations_, Oxford University Press, 1977.

27. L.M. Delves and J. Walsh (eds.), _Numerical Solution of Integral Equations_, Oxford University Press, 1974.

28. R. Weiss and R.S. Anderssen, "A Product Integration Method for a Class of Singular First Kind Volterra Equations," _Numerishe Mathematik_, Vol. 18, 1972, pp. 442-456.

29. P.J. Davis and P. Rabinowitz, _Methods of Numerical Integration_, 2nd Edition, Academic Press, 1984.

30. L.J. Jacobs, W.R. Scott, D.M. Granata and M.J. Ryan, "Acoustic Emission from a Crack Growth Event," presented at the 15th Annual Review of Progress in Quantitative Nondestructive Evaluation, 1988.

SESSION 36 - SPECIAL PANEL SESSION

ARMY RESEARCH THRUST AREAS & OPPORTUNITIES FOR ADVANCES IN STRUCTURES, STRUCTURAL DYNAMICS & MATERIALS

Dr. Robert E. Singleton
U.S. Army Research Office

RESEARCH OPPORTUNITIES
STRUCTURES & DYNAMICS

- VIBRATION PREDICTION/SUPPRESSION

- SMART STRUCTURES

- STRUCTURAL COUPLINGS

- MULTI-BODY DYNAMICS

- NONLINEAR STRUCTURAL RESPONSE

- MACHINE/MECHANISM SYSTEMS

ARO

ENGINEERING SCIENCES DIVISION

STRUCTURES AND DYNAMICS PROGRAM

INNOVATIVE VIBRATION SUPPRESSION TECHNIQUES

** *NOVEL CONTROL TECHNIQUES*
** *INTELLIGENT STRUCTURES*

- Vibrational Control
- Distributed Thermal Actuators
- Composite Materials Incorporating Electro—Rheological Fluids
- Composite Materials that Contain Shape Memory Alloy In
    Fiber Form
- Hygrothermoelastic Effects In Laminated Composites
- Piezoelectric Material Actuators Embedded In Homogeneous
    and Composite Materials

ARO

ENGINEERING SCIENCES DIVISION
STRUCTURES AND DYNAMICS PROGRAM

US ARMY RESEARCH OFFICE

POTENTIAL VIBRATION SUPPRESSION TECHNIQUES

- Higher Harmonic Control

- Individual Blade Control

- Vibrational Control

- "Intelligent" Structures:
  Laminated Composite Materials

  ★ Hygrothermoelastic Effects

  ★ Embedded Thermal Actuators

  ★ Embedded Piezoelectric Ceramics and Films

ARO

ENGINEERING SCIENCES DIVISION
STRUCTURES AND DYNAMICS PROGRAM

HIGHER HARMONIC CONTROL OF HELICOPTER VIBRATIONS

Vibration Suppression in Helicopters

SENSOR UNIT NO. 3
SENSOR UNIT NO. 4
HHC CONTROLLER
PRIMARY FBW ACTUATORS
LHX CENTRAL CONTROL/MISSION MANAGEMENT
SENSOR UNIT NO. 2
SENSOR UNIT NO. 1
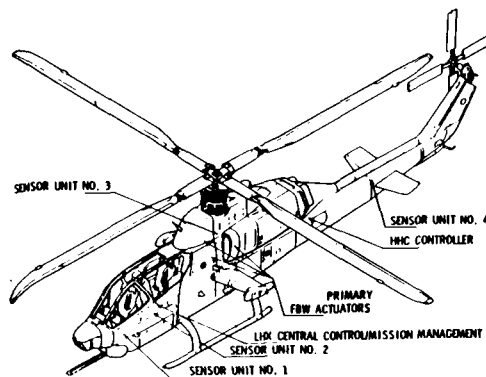
Planned locations of HHC equipment.

ARO

ENGINEERING SCIENCES DIVISION

STRUCTURES AND DYNAMICS PROGRAM

US ARMY LABORATORY COMMAND

US ARMY RESEARCH OFFICE

INTELLIGENT STRUCTURES

Embedded and/or Distributed Sensors

- Strain

- Thermal Gradients

- Piezoelectric Crystals, Ceramics, and Films

- Electro-Rheological Fluids
  (solid and liquid phases)

- Shape Memory Alloy Wires (e.g., nitinol)

- Fiber Optics

ARO

ENGINEERING SCIENCES DIVISION

STRUCTURES AND DYNAMICS PROGRAM

VIBRATION CONTROL OF FLEXIBLE STRUCTURES USING PIEZOELECTRIC DEVICES AS SENSORS AND ACTUATORS

PRINCIPLE

- Apply a voltage to the piezoelectric ceramic.
- Electric field creates a mechanical deformation in the sub-structure.
- Damping is obtained from the rate feedback to the piezoelectric actuator.
- Vibration suppression is realized.

FEEDBACK ELECTRONICS

ALUMINUM

GRAPHITE/EPOXY

GLASS/EPOXY
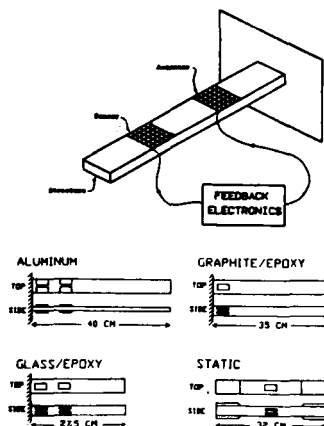
STATIC

Dynamic and static test specimens (side view not to scale).

ARO

ENGINEERING SCIENCES DIVISION
STRUCTURES AND DYNAMICS PROGRAM

A COMPOSITE STRUCTURE CONTAINING AN ERF
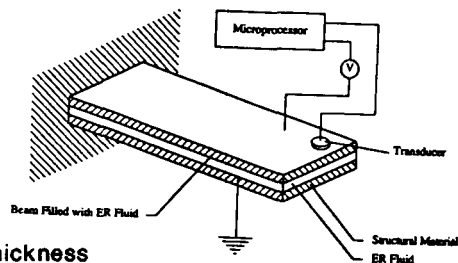
Voltage Required: 4 kV/mm of fluid thickness
Current Density: 10 μA/cm^2
==> Total *POWER* required is quite low.

Response Time to Voltage Excitation: < 1 msec

Increase in Structural Stiffness: 30 - 40%

GOAL - Integrate fundamental phenomenological
theories (*fluid-structure interaction*) with
● *Intelligent Sensor Technologies*
● *Modern Control Strategies*

ARO

ENGINEERING SCIENCES DIVISION
STRUCTURES AND DYNAMICS PROGRAM

INTELLIGENT STRUCTURES
ELECTRORHEOLOGICAL FLUIDS

Applications for ERFs in structures are foreseen in

■ Helicopter Rotors

■ Adaptive Suspension Vehicles

■ Robotization of Ammunition
Supply and Materiel Handling
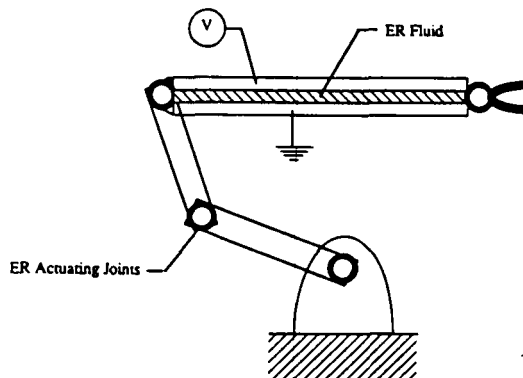
DYNAMIC PROPERTIES OF COMPOSITE BLADES WITH STRUCTURAL COUPLINGS

x, y, z : undeformed
x', y', z' : deformed
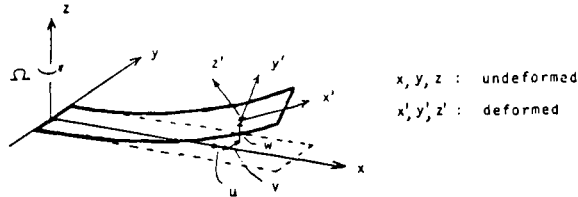
OBJECTIVES

- To provide improved methods for analysis and design of aeroelastically tailored composite rotor blades for the next generation of helicopters.

- To develop criteria for the structural dynamic characteristics of these blades under a wide variety of configurations.

VIBRATION CONTROL IN COMPOSITE STRUCTURES THROUGH APPLICATION OF ADD—ON DAMPING MATERIALS

OBJECTIVES
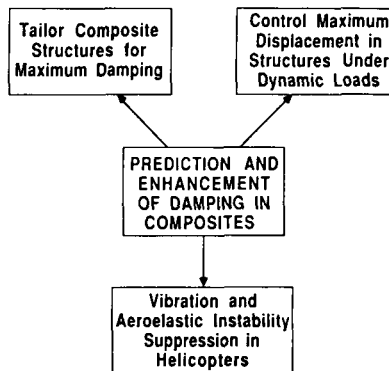
Tailor Composite Structures for Maximum Damping

Control Maximum Displacement in Structures Under Dynamic Loads

PREDICTION AND ENHANCEMENT OF DAMPING IN COMPOSITES

Vibration and Aeroelastic Instability Suppression in Helicopters

APPLICATIONS OF CONCEPTS OF MULTI—BODY DYNAMICS TO DESIGN AND OPTIMIZATION OF

- **Weapon Systems**
- **Earth Vehicles (Tanks, Trucks, Etc.)**
- **Rotorcraft (Helicopters, Tiltrotor Craft)**

APPLICATION OF MULTI-BODY DYNAMICS TO DEFORMABLE MECHANISMS
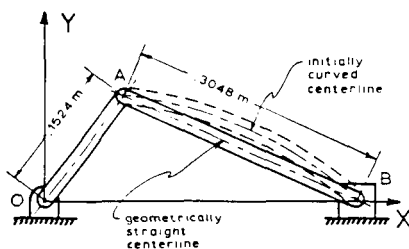
Slider-Crank Mechanism
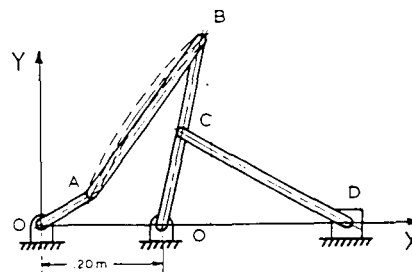
Six-Bar Mechanism

ARO

ENGINEERING SCIENCES DIVISION

STRUCTURES AND DYNAMICS PROGRAM

SPATIAL DYNAMICS OF DEFORMABLE MULTIBODY SYSTEMS WITH VARIABLE KINEMATIC STRUCTURE

MULTIBODY SYSTEMS

* Component Connectivity

* Component Flexibility

* Impact

* Impulsive Forces

* Change in the System Topology

ARO
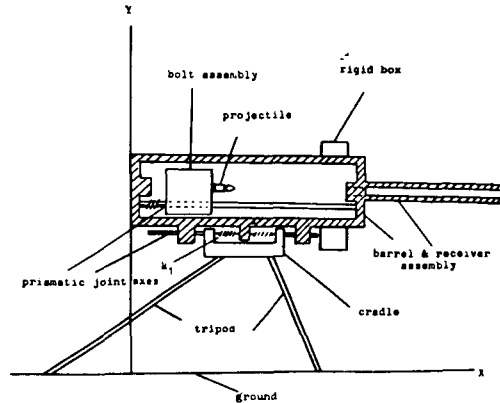
ENGINEERING SCIENCES DIVISION

STRUCTURES AND DYNAMICS PROGRAM

NONLINEAR OSCILLATIONS OF MECHANICAL SYSTEMS UNDER MULTIFREQUENCY PARAMETRIC EXCITATION

Most previous work has been restricted to single-frequency excitation:
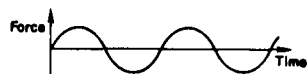
Many dynamic forces involve multiple frequencies:
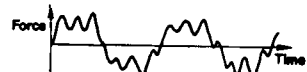
Random forces can be approximated by multi-frequency excitation.
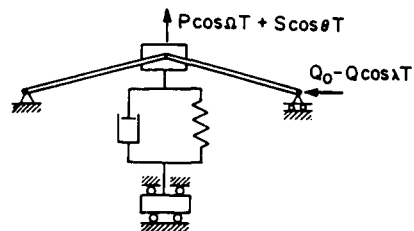
## DYNAMIC STABILITY OF FLEXIBLE
ROBOT MANIPULATORS

GOALS

★ Achieve stability of motion and computer control of precise positioning of fast, light weight, deformable robot arms, military aiming devices, and robotic tank autoloaders.

★ Explore stability of motion problems associated with robot arm equiped military vehicles.

★ Perform experimental simulation of the motion of a deformable robot attached to a moving base.

FUTURE THRUSTS — MATERIALS

- Protective Coatings & Barrier Materials
- Advanced Ceramics & Composites for High Loading Rate Regimes
- Manufacturing & Processing Science
- Supercritical Fluids
- Novel Magnetic Materials
- Nondestructive Evaluation of Materials
- New Aspects of Hierarchical Structures
    Bio-Systems ——▶ Optical, Thermal
- Artificially Structured Materials
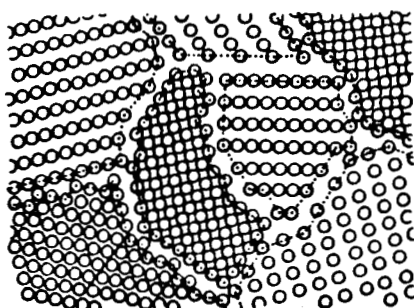- Non-Linear & Gradient Optic Materials

HIGH STRENGTH
REINFORCED COMPOSITES
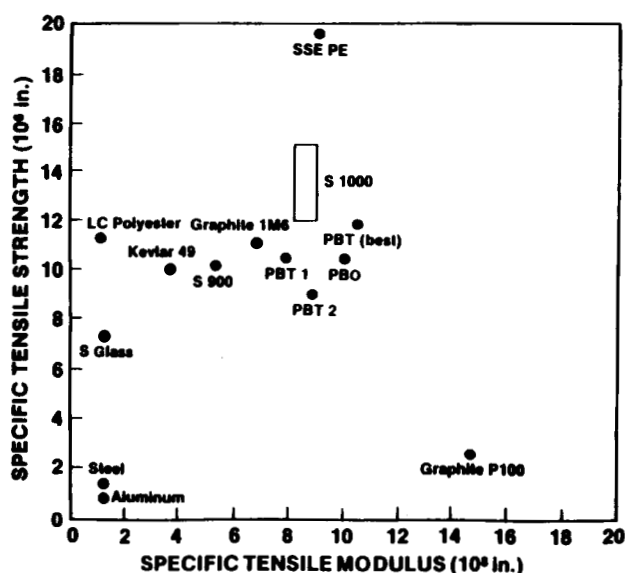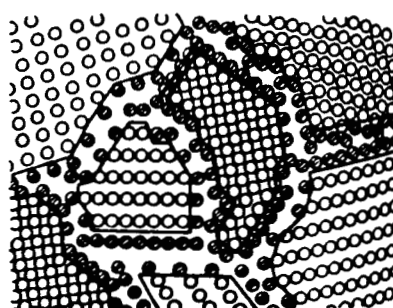

LIGHT WEIGHT HELMETS

**BRADLEY FIGHTING VEHICLE
COMPOSITE HULL**

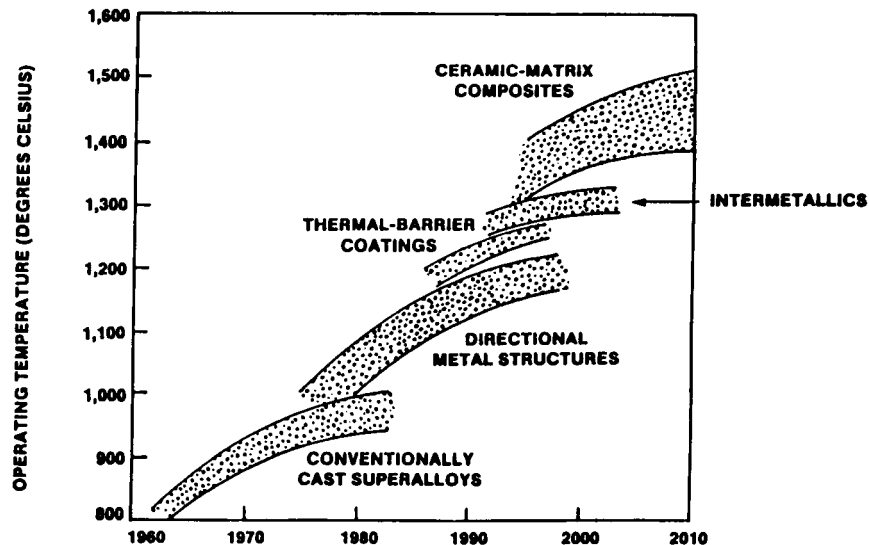# NANOCRYSTALLINE MATERIALS
(MICROSTRUCTURAL REPRESENTATION)
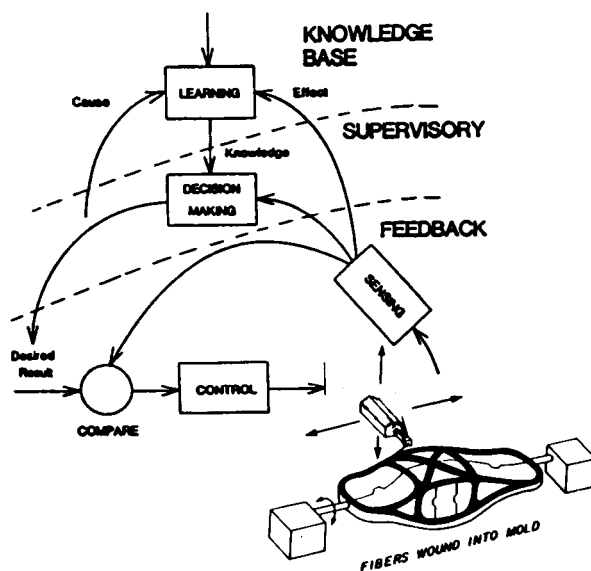

POLYCRYSTALLINE MATERIAL

NANOPHASE MATERIAL

Open Circles – Crystalline Grain Atoms
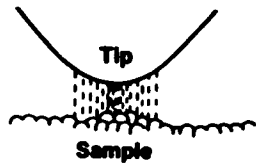
Cross-Hatched Circles – Grain Boundary Atoms

88

OPERATIONAL TEMPERATURES
OF ADVANCED MATERIALS

MANUFACTURING SCIENCE

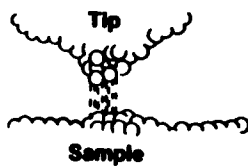- LIFE EXTENSION - 200-300%
- RELIABILITY - 100%
- MAINTAINABILITY - 75%
- COST SAVINGS - 50%
- DESIGN VERSATILITY
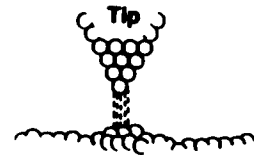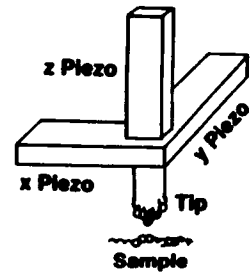
8

SCANNING TUNNELING MICROSCOPY

Tip

Sample

The plan

Tip

Sample

The discovery

Tip

Sample

The idea

z Piezo

y Piezo

x Piezo

Tip

Sample

The instrument

ORIGINAL PAGE
BLACK AND WHITE PHOTOGRAPH

NASA
National Aeronautics and
Space Administration

Report Documentation Page

1. Report No.	2. Government Accession No.	3. Recipient's Catalog No.
NASA CP-10024		

4. Title and Subtitle	5. Report Date
Research in Structures, Structural Dynamics and Materials - 1989	April 1989
	6. Performing Organization Code

7. Author(s)	8. Performing Organization Report No.
William F. Hunter and Ahmed K. Noor, Compilers	
	10. Work Unit No.
	505-63-21-02

9. Performing Organization Name and Address	11. Contract or Grant No.
NASA Langley Research Center Hampton, Virginia 23665-5225	
	13. Type of Report and Period Covered

12. Sponsoring Agency Name and Address	Conference Publication
National Aeronautics and Space Administration Washington, DC 20546-0001	14. Sponsoring Agency Code

15. Supplementary Notes

Primarily Viewgraphs
William F. Hunter: Langley Research Center, Hampton, Virginia
Ahmed K. Noor: George Washington University - Joint Institute for
                   Advancement of Flight Sciences, Hampton, Virginia

16. Abstract

   The AIAA/ASME/ASCE/AHS/ASC 30th Structures, Structural Dynamics and Materials (SDM) Conference was held on April 3-5, 1989 in Mobile, Alabama. This publication is a compilation of presentations of the Work-In-Progress sessions and presentations or papers by invited speakers for special sessions. This publication does not contain papers from the regular sessions since those papers are published by AIAA in the conference proceedings.

17. Key Words (Suggested by Author(s))	18. Distribution Statement
SDM Conference Work-In-Progress Structures Structural Dynamics Materials	Unclassified-Unlimited Subject Category 39

19. Security Classif. (of this report)	20. Security Classif. (of this page)	21. No. of pages	22. Price
Unclassified	Unclassified	96	A05

SESSION 6 - WORK-IN-PROGRESS I